Chapter 9

SPIN WAVES IN SYSTEMS WITH LONG RANGE INTERACTION

9.1. Dipole–Dipole Interaction

In the previous chapters, we have studied magnetic systems where the spins are interacting via an exchange interaction that was not extended beyond a few shell of neighbours. This is well justified for the magnetic compounds with a high critical temperature indicating that the interaction between the spins originates from the exchange interaction. In these compounds, any other magnetic interaction can be neglected if one is interested to investigate their low temperature magnetic properties. However, the long range dipole–dipole interaction is always present in magnetic compounds and its effect becomes important in the vicinity of the critical point where the choice of the "universality class" in a continuous phase transition depends on the short or long range nature of the interaction. On the other hand, when the exchange interaction is very weak (comparable with the dipolar interaction) as for some quasi-1D or quasi-2D magnetic systems, the dipole–dipole interaction plays a crucial role in determining the magnetic LRO. Such magnetic systems are characterized by very low magnetic critical temperature as for some HTCS[61] like $RBa_2Cu_3O_{6+x}$ where[79] R is a rare earth (R = Dy, Er, Nd) that show an ordered magnetic phase at temperatures below $T_N \sim 1\,\mathrm{K}$ depending on the oxygenation x. For instance,[79] the fully oxygenated $ErBa_2Cu_3O_7$ ($x = 1$) is a superconductor ($T_c = 92\,\mathrm{K}$) with a Néel temperature $T_N = 0.62\,\mathrm{K}$ while the deoxygenated $ErBa_2Cu_3O_6$ ($x = 0$) is an insulator without long range 3D magnetic order. In the fully oxygenated sample ($x = 1$), the magnetic Er^{3+} ions crystallize in an orthorhombic lattice[79] with $a = 3.82\,\text{Å}$, $b = 3.88\,\text{Å}$ and $c = 11.66\,\text{Å}$ while in the deoxygenate sample ($x \simeq 0$) the Er^{3+} ions crystallize[80] in a tetragonal lattice with $a = b = 3.85\,\text{Å}$ and $c = 11.79\,\text{Å}$. In the ordered magnetic phase of the oxygenated sample, the magnetic moments of the Er^{3+} ions are aligned along the b-axis forming ferromagnetic chains along the b-axis and antiferromagnetic chains along the a-axis. Along the c-axis, both ferromagnetic and antiferromagnetic orders have been found.[79] Either the very low Néel temperature and the kind of order found in the ordered phase cannot be explained in terms of a NN exchange Hamiltonian.

As an example of quasi-1D ferromagnet, we point out the compound[81] $CsNiF_3$, a member of the large family of magnetic systems ABX_3 where A is an alkali metal, B a transition metal and X a halogen. The magnetic Ni^{2+} ($S = 1$) ions crystallize in the H lattice with $a = b = 6.21\,\text{Å}$ and $c = 2.9\,\text{Å}$ and are ferromagnetically coupled along the c-axis (chain) by an exchange interaction $J/k_B = 11.8\,\text{K}$. The antiferromagnetic coupling between the chains J' is about 500 times smaller than the intrachain coupling so that it is of the same order of magnitude of the dipolar interaction. The crucial role of the dipole–dipole interaction is pointed out by the very low transition temperature ($T_N = 2.67\,\text{K}$) and by the kind of order found in the ordered phase. Indeed, the antiferromagnetic order found in the ab-planes does not correspond to the expected 120°-phase of a NN Heisenberg antiferromagnet.

From a theoretical point of view, the dipolar interaction is interesting for two reasons:

i) the long range nature of the dipole–dipole interaction rules out the application of the Mermin and Wagner theorem[22] according to which the LRO is prevented at any finite temperature for Heisenberg or planar rotator models with short range interaction;
ii) the anisotropic nature of the dipole–dipole interaction changes the symmetry of the isotropic Hamiltonian choosing an easy-axis (Ising model) or an easy-plane (planar model) depending on the lattice structure.

The dipolar Hamiltonian is given by

$$\mathcal{H}_{\text{dip}} = -\frac{1}{2}\sum_{i\neq j}\frac{1}{r_{ij}^3}\left[3\frac{(\boldsymbol{\mu}_i\cdot\boldsymbol{r}_{ij})(\boldsymbol{\mu}_j\cdot\boldsymbol{r}_{ij})}{r_{ij}^2} - \boldsymbol{\mu}_i\cdot\boldsymbol{\mu}_j\right], \tag{9.1.1}$$

where i, j run over all sites of the lattice, $\boldsymbol{r}_{ij}$ is the lattice vector joining the points i and j and $\boldsymbol{\mu}_i$ is the magnetic moment located at site i. Replacing the magnetic moments $\boldsymbol{\mu}_i$ by $g\mu_B\boldsymbol{S}_i$ where g is the Landé factor and μ_B the Bohr magneton and writing the lattice site $\boldsymbol{r}_j$ as $\boldsymbol{r}_i + \boldsymbol{r}$, the Hamiltonian (9.1.1) becomes

$$\mathcal{H}_{\text{dip}} = -\frac{(g\mu_B)^2}{2}\sum_{\alpha,\beta}\sum_i\sum_{\boldsymbol{r}\neq 0}\frac{1}{r^3}\left[3\frac{r_\alpha r_\beta}{r^2} - \delta_{\alpha,\beta}\right]S_i^\alpha S_{i+\boldsymbol{r}}^\beta, \tag{9.1.2}$$

where α, β run over the cartesian crystallographic axes x, y, z. If the lattice is supposed to be infinite, the choice of the origin from which to measure the lattice vector $\boldsymbol{r}$ is independent of i so that the sum over $\boldsymbol{r}$ is similar to the sum over i except that $\boldsymbol{r} \neq 0$. In the following, we limit ourselves to account for spiral configurations. Then we introduce a reference system of local axes ξ, η, ζ in the same way as in Chapter 7. The ground-state spin configuration is then given by

$$\begin{aligned} S_i^x &= S\sin\theta\cos\ \phi_i, \\ S_i^y &= S\sin\theta\sin\ \phi_i, \\ S_i^z &= S\cos\theta \end{aligned} \tag{9.1.3}$$

with $\phi_i = \boldsymbol{Q}\cdot\boldsymbol{r}_i + \phi$ and the corresponding ground-state energy is

$$E_{\rm dip} = -\frac{(g\mu_B S)^2}{2}\sum_i\sum_{\boldsymbol{r}\neq 0}\frac{1}{r^3}\left\{\left(3\frac{r_z^2}{r^2}-1\right)\cos^2\theta + \left[3\frac{r_x r_y}{r^2}\sin(\phi_i+\phi_{i+\boldsymbol{r}})\right.\right.$$
$$+\left(3\frac{r_x^2}{r^2}-1\right)\cos\phi_i\cos\phi_{i+\boldsymbol{r}} + \left(3\frac{r_y^2}{r^2}-1\right)\sin\phi_i\sin\phi_{i+\boldsymbol{r}}\left.\right]\sin^2\theta$$
$$\left.+\frac{3r_z}{r^2}[r_x\cos(\phi_i+\phi_{i+\boldsymbol{r}}) + r_y(\sin\phi_i+\sin\phi_{i+\boldsymbol{r}})]\sin\theta\cos\theta\right\}. \qquad (9.1.4)$$

By using the relationship

$$\sum_i e^{i\boldsymbol{Q}\cdot\boldsymbol{r}_i} = N\delta_{\boldsymbol{Q},\boldsymbol{G}}, \qquad (9.1.5)$$

where $\boldsymbol{G}$ is a reciprocal lattice vector, the sum over i in Eq. (9.1.4) can be performed leading to

$$E_{\rm dip}(\theta,\boldsymbol{Q},\phi) = -\frac{(g\mu_B S)^2}{2}N\left\{D^{zz}(0)\cos^2\theta + \left[\frac{1}{2}\left(D^{xx}\left(\frac{\boldsymbol{G}}{2}\right)\right.\right.\right.$$
$$\left.-D^{yy}\left(\frac{\boldsymbol{G}}{2}\right)\right)\delta_{\boldsymbol{Q},\frac{\boldsymbol{G}}{2}}\cos 2\phi + \frac{1}{2}(D^{xx}(\boldsymbol{Q})+D^{yy}(\boldsymbol{Q}))$$
$$\left.+D^{xy}\left(\frac{\boldsymbol{G}}{2}\right)\delta_{\boldsymbol{Q},\frac{\boldsymbol{G}}{2}}\sin 2\phi\right]\sin^2\theta + 2\left(D^{xz}(0)\cos\phi\right.$$
$$\left.+D^{yz}(0)\sin\phi\right)\delta_{\boldsymbol{Q},0}\sin\theta\cos\theta\Big\}, \qquad (9.1.6)$$

where

$$D^{\alpha\beta}(\boldsymbol{Q}) = \sum_{\boldsymbol{r}\neq 0}\frac{e^{i\boldsymbol{Q}\cdot\boldsymbol{r}}}{r^3}\left(3\frac{r_\alpha r_\beta}{r^2}-\delta_{\alpha,\beta}\right). \qquad (9.1.7)$$

Equation (9.1.6) is correct for Bravais lattices for which $D^{\alpha\beta}(\boldsymbol{Q}) = D^{\alpha\beta}(-\boldsymbol{Q})$. From Eq. (9.1.7), it is direct to obtain the "sum rule"

$$D^{xx}(\boldsymbol{Q}) + D^{yy}(\boldsymbol{Q}) + D^{zz}(\boldsymbol{Q}) = 0 \qquad (9.1.8)$$

and $D^{\alpha\beta}(0) = 0$ for any $\alpha \neq \beta$. Using the sum rule (9.1.8), the dipolar energy (9.1.6) becomes

$$E_{\rm dip}(\theta,\boldsymbol{Q},\phi) = -\frac{(g\mu_B S)^2}{2}N\left\{D^{zz}(0)\cos^2\theta - \frac{1}{2}D^{zz}(\boldsymbol{Q})\sin^2\theta\right.$$
$$+\frac{1}{2}\left[\left(D^{xx}\left(\frac{\boldsymbol{G}}{2}\right)-D^{yy}\left(\frac{\boldsymbol{G}}{2}\right)\right)\cos 2\phi\right.$$
$$\left.\left.+D^{xy}\left(\frac{\boldsymbol{G}}{2}\right)\sin 2\phi\right]\delta_{\boldsymbol{Q},\frac{\boldsymbol{G}}{2}}\sin^2\theta\right\}, \qquad (9.1.9)$$

where the parameters θ, $\boldsymbol{Q}$ and ϕ have to be determined minimizing the ground-state energy (9.1.9). Unlike the isotropic exchange Hamiltonian (7.1.4), in the

ground-state energy (9.1.9), the angle ϕ does appear pointing out the anisotropic nature of the dipole–dipole interaction. The possible minima of the function (9.1.9) correspond to

i) ferromagnetic configuration with the spins directed along the x-axis ($\theta = \frac{\pi}{2}$, $\phi = 0$, $\boldsymbol{Q} = 0$) or along the y-axis ($\theta = \frac{\pi}{2}$, $\phi = \frac{\pi}{2}$, $\boldsymbol{Q} = 0$) or along the z-axis ($\theta = 0$) whose energy is given by

$$E^{\alpha}_{\rm dip}(0) = -\frac{(g\mu_B S)^2}{2} N D^{\alpha\alpha}(0) \tag{9.1.10}$$

with $\alpha = x, y, z$, respectively;

ii) antiferromagnetic configuration with the spins directed along the x-axis ($\theta = \frac{\pi}{2}$, $\phi = 0$, $\boldsymbol{Q} = \frac{\boldsymbol{G}}{2}$) or along the y-axis ($\theta = \frac{\pi}{2}$, $\phi = \frac{\pi}{2}$, $\boldsymbol{Q} = \frac{\boldsymbol{G}}{2}$) whose energy is given by

$$E^{\alpha}_{\rm dip}\left(\frac{\boldsymbol{G}}{2}\right) = -\frac{(g\mu_B S)^2}{2} N D^{\alpha\alpha}\left(\frac{\boldsymbol{G}}{2}\right) \tag{9.1.11}$$

with $\alpha = x, y$, respectively. As one can see from Eqs. (9.1.10) and (9.1.11), the dipolar interaction selects both the kind of magnetic order and the spin direction of the ground-state configuration. When $\boldsymbol{Q} \neq 0$, the long range character of the dipole–dipole interaction does not affect dramatically the sums (9.1.7) since the oscillating nature of the cosine function balances the long range of the dipolar interaction. On the contrary, for $\boldsymbol{Q} = 0$ the sums (9.1.7) are very slowly convergent: when they are restricted to a finite sample they depend on the shape of the sample. In the next section, we will evaluate explicitly the sums (9.1.7) with $\boldsymbol{Q} = 0$ for a spherical sample.

9.2. Dipolar Sums and Ewald's Method

Let us evaluate explicitly the sums (9.1.7) for an infinite 3D lattice following the Ewald's method.[82] The main problem of the sums (9.1.7) is that they are very slowly convergent. The Ewald's method consists on transforming such slowly convergent sums into quickly convergent sums entering generalized functions that decrease rapidly as their arguments increase. To do this, one splits the original sum in two parts: the former sum is extended to the direct lattice vectors while the latter sum is transformed in a sum over the reciprocal lattice vectors. We treat separately the two terms occurring in the sums (9.1.7). Let us begin with the last term of (9.1.7) and use the identity

$$\sum_{l\neq 0} \frac{e^{i\boldsymbol{Q}\cdot\boldsymbol{r}_l}}{r_l^3} = \frac{4}{\sqrt{\pi}} \sum_{l\neq 0} e^{i\boldsymbol{Q}\cdot\boldsymbol{r}_l} \int_0^{\infty} dz\ z^2 e^{-r_l^2 z^2} \equiv \frac{4}{\sqrt{\pi}}(A + B), \tag{9.2.1}$$

where

$$A = \sum_{l\neq 0} e^{i\boldsymbol{Q}\cdot\boldsymbol{r}_l} \int_0^{\eta} dz\ z^2 e^{-r_l^2 z^2} = -\frac{1}{3}\eta^3 + \sum_{l} e^{i\boldsymbol{Q}\cdot\boldsymbol{r}_l} \int_0^{\eta} dz\ z^2 e^{-r_l^2 z^2} \tag{9.2.2}$$

and

$$B = \sum_{l\neq 0} e^{i\boldsymbol{Q}\cdot\boldsymbol{r}_l} \int_\eta^\infty dz\, z^2 e^{-r_l^2 z^2} = \eta^3 \sum_{l\neq 0} e^{i\boldsymbol{Q}\cdot\boldsymbol{r}_l} \frac{1}{(\eta r_l)^3} \int_{\eta r_l}^\infty dt\; t^2 e^{-t^2}. \tag{9.2.3}$$

Taking advantage from the theta-function transformation[82]

$$\sum_l z^3 e^{i\boldsymbol{Q}\cdot\boldsymbol{r}_l} e^{-r_l^2 z^2} = \rho\pi^{3/2} \sum_l e^{-\frac{(\boldsymbol{G}_l+\boldsymbol{Q})^2}{4z^2}}, \tag{9.2.4}$$

where the first sum runs over the direct lattice vectors $\boldsymbol{r}_l$ while the second sum runs over the reciprocal lattice vectors $\boldsymbol{G}_l$ with $\rho = 1/v_c$, v_c being the unit cell volume, Eq. (9.2.2) becomes

$$A = -\frac{1}{3}\eta^3 + \rho\pi^{3/2} \sum_l \int_0^\eta \frac{dz}{z} e^{-\frac{(\boldsymbol{G}_l+\boldsymbol{Q})^2}{4z^2}} = -\frac{1}{3}\eta^3 - \frac{1}{2}\rho\pi^{3/2} \sum_l \mathrm{Ei}\left[-\frac{(\boldsymbol{G}_l+\boldsymbol{Q})^2}{4\eta^2}\right], \tag{9.2.5}$$

where the change of variable $z = \frac{|\boldsymbol{G}_l+\boldsymbol{Q}|}{2\sqrt{t}}$ has been performed in Eq. (9.2.5) and

$$\mathrm{Ei}\left(-x^2\right) = -\int_{x^2}^\infty dt \frac{e^{-t}}{t} \tag{9.2.6}$$

is the exponential integral function.[4] Equation (9.2.3) may be written

$$B = \frac{1}{2}\eta^3 \sum_{l\neq 0} e^{i\boldsymbol{Q}\cdot\boldsymbol{r}_l} f_B\left(\eta r_l\right) \tag{9.2.7}$$

where

$$f_B(x) = \frac{2}{x^3} \int_x^\infty dz\; z^2 e^{-z^2} = \frac{e^{-x^2}}{x^2} + \frac{\sqrt{\pi}}{2x^3}\,\mathrm{erfc}(x) \tag{9.2.8}$$

and

$$\mathrm{erfc}(x) = \frac{2}{\sqrt{\pi}} \int_x^\infty dt\; e^{-t^2} \tag{9.2.9}$$

is the complementary error function.[4] Replacing Eqs. (9.2.5) and (9.2.7) into Eq. (9.2.1), one obtains

$$\sum_{l\neq 0} \frac{e^{i\boldsymbol{Q}\cdot\boldsymbol{r}_l}}{r_l^3} = -\frac{4\eta^3}{3\sqrt{\pi}} - 2\pi\rho \sum_l \mathrm{Ei}\left[-\frac{(\boldsymbol{G}_l+\boldsymbol{Q})^2}{4\eta^2}\right] + \frac{2\eta^3}{\sqrt{\pi}} \sum_{l\neq 0} e^{i\boldsymbol{Q}\cdot\boldsymbol{r}_l} f_B(\eta r_l). \tag{9.2.10}$$

In order to evaluate the first term of the sums (9.1.7), we use the relationship

$$\sum_{l\neq 0} \frac{e^{i\boldsymbol{Q}\cdot\boldsymbol{r}_l}}{r_l^5} r_l^\alpha r_l^\beta = -\frac{\partial^2}{\partial Q_\alpha \partial Q_\beta} \sum_{l\neq 0} \frac{e^{i\boldsymbol{Q}\cdot\boldsymbol{r}_l}}{r_l^5} \tag{9.2.11}$$

and the identity

$$\sum_{l\neq 0} \frac{e^{i\boldsymbol{Q}\cdot\boldsymbol{r}_l}}{r_l^5} = \frac{8}{3\sqrt{\pi}} \sum_{l\neq 0} e^{i\boldsymbol{Q}\cdot\boldsymbol{r}_l} \int_0^\infty dz\; z^4 e^{-r_l^2 z^2} \equiv \frac{8}{3\sqrt{\pi}}\,(C+D), \tag{9.2.12}$$

where

$$C = \sum_{l\neq 0} e^{i\boldsymbol{Q}\cdot\boldsymbol{r}_l} \int_0^\eta dz\, z^4 e^{-r_l^2 z^2} = -\frac{1}{5}\eta^5 + \sum_l e^{i\boldsymbol{Q}\cdot\boldsymbol{r}_l} \int_0^\eta dz z^4 e^{-r_l^2 z^2}$$
$$= -\frac{1}{5}\eta^5 + \frac{1}{2}\rho\pi^{3/2}\eta^2 \sum_l f_C\left[\frac{(\boldsymbol{G}_l+\boldsymbol{Q})^2}{4\eta^2}\right] \quad (9.2.13)$$

with

$$f_C(x^2) = x^2 \int_{x^2}^\infty \frac{dt}{t^2} e^{-t^2} = e^{-x^2} + x^2 \mathrm{Ei}(-x^2) \quad (9.2.14)$$

and

$$D = \sum_{l\neq 0} e^{i\boldsymbol{Q}\cdot\boldsymbol{r}_l} \int_\eta^\infty dz z^4 e^{-r_l^2 z^2} = \frac{1}{2}\eta^5 \sum_{l\neq 0} e^{i\boldsymbol{Q}\cdot\boldsymbol{r}_l} f_D(\eta r_l) \quad (9.2.15)$$

where

$$f_D(x) = \frac{2}{x^5}\int_x^\infty dt\ t^4 e^{-t^2} = \frac{3+2x^2}{2x^4} e^{-x^2} + \frac{3\sqrt{\pi}}{4x^5}\mathrm{erfc}(x). \quad (9.2.16)$$

Replacing Eqs. (9.2.13) and (9.2.15) into Eq. (9.2.12), one obtains

$$\sum_{l\neq 0} \frac{e^{i\boldsymbol{Q}\cdot\boldsymbol{r}_l}}{r_l^5} = -\frac{8\eta^5}{15\sqrt{\pi}} + \frac{4\pi}{3}\rho\eta^2 \sum_l f_C\left[-\frac{(\boldsymbol{G}_l+\boldsymbol{Q})^2}{4\eta^2}\right] + \frac{4\eta^5}{3\sqrt{\pi}} \sum_{l\neq 0} e^{i\boldsymbol{Q}\cdot\boldsymbol{r}_l} f_D(\eta r_l). \quad (9.2.17)$$

From the relationship (9.2.11), one obtains

$$\sum_{l\neq 0} \frac{e^{i\boldsymbol{Q}\cdot\boldsymbol{r}_l}}{r_l^5} r_l^\alpha r_l^\beta = -\frac{2\pi}{3}\rho\delta_{\alpha,\beta} \sum_l \mathrm{Ei}\left[\frac{-(\boldsymbol{G}_l+\boldsymbol{Q})^2}{4\eta^2}\right]$$
$$- \frac{4\pi}{3}\rho \sum_l \frac{(\boldsymbol{G}_l+\boldsymbol{Q})_\alpha (\boldsymbol{G}_l+\boldsymbol{Q})_\beta}{(\boldsymbol{G}_l+\boldsymbol{Q})^2} e^{-\frac{(\boldsymbol{G}_l+\boldsymbol{Q})^2}{4\eta^2}}$$
$$+ \frac{4\eta^5}{3\sqrt{\pi}} \sum_{l\neq 0} r_l^\alpha r_l^\beta e^{i\boldsymbol{Q}\cdot\boldsymbol{r}_l} f_D(\eta r_l). \quad (9.2.18)$$

Finally, replacing Eqs. (9.2.10) and (9.2.18) into the sums (9.1.7) one obtains

$$D_\infty^{\alpha\beta}(\boldsymbol{Q}) = -4\pi\rho \sum_l \frac{(\boldsymbol{G}_l+\boldsymbol{Q})_\alpha (\boldsymbol{G}_l+\boldsymbol{Q})_\beta}{(\boldsymbol{G}_l+\boldsymbol{Q})^2} e^{-\frac{(\boldsymbol{G}_l+\boldsymbol{Q})^2}{4\eta^2}} + \frac{4\eta^5}{\sqrt{\pi}} \sum_{l\neq 0} r_l^\alpha r_l^\beta e^{i\boldsymbol{Q}\cdot\boldsymbol{r}_l} f_D(\eta r_l)$$
$$+ \frac{2\eta^3}{\sqrt{\pi}}\delta_{\alpha,\beta}\left[\frac{2}{3} - \sum_{l\neq 0} e^{i\boldsymbol{Q}\cdot\boldsymbol{r}_l} f_B(\eta r_l)\right], \quad (9.2.19)$$

where the subscript ∞ means that the original dipolar sums on the left-hand side of (9.2.19) can be replaced by the generalized functions occurring in the right-hand side

only for infinite lattices. Indeed, the theta-function transformation (9.2.4) implies an infinite sum over both the direct and the reciprocal lattice vectors. Equation (9.2.19) was given by Cohen and Keffer.[83] Notice the quick convergence of the series on the right-hand side of Eq. (9.2.19) due to the generalized functions $f_D(x) \simeq f_B(x) \simeq \frac{e^{-x^2}}{x^2}$ for $x \to \infty$. An interesting result is obtained for $\boldsymbol{Q} \to 0$. Indeed,

$$\lim_{\boldsymbol{Q}\to 0} D_\infty^{\alpha\beta}(\boldsymbol{Q}) = -4\pi\rho \left[\frac{Q_\alpha Q_\beta}{Q^2} + \sum_{l\neq 0} \frac{G_l^\alpha G_l^\beta}{G_l^2} e^{-\frac{G_l^2}{4\eta^2}} \right] + \frac{4\eta^5}{3\sqrt{\pi}} \sum_{l\neq 0} r_l^\alpha r_l^\beta f_D(\eta r_l) + \frac{2\eta^3}{\sqrt{\pi}} \delta_{\alpha,\beta} \left[\frac{2}{3} - \sum_{l\neq 0} f_B(\eta r_l) \right]. \quad (9.2.20)$$

For the lattices we are interested to (for instance, cubic, tetragonal, orthorhombic), one has

$$\sum_{l\neq 0} \frac{G_l^\alpha G_l^\beta}{G_l^2} e^{-\frac{G_l^2}{4\eta^2}} = \delta_{\alpha,\beta} \sum_{l\neq 0} \frac{(G_l^\alpha)^2}{G_l^2} e^{-\frac{G_l^2}{4\eta^2}} \quad (9.2.21)$$

and

$$\sum_{l\neq 0} r_l^\alpha r_l^\beta f_D(\eta r_l) = \delta_{\alpha,\beta} \sum_{l\neq 0} (r_l^\alpha)^2 f_D(\eta r_l) \quad (9.2.22)$$

so that Eq. (9.2.20) becomes

$$\lim_{\boldsymbol{Q}\to 0} D_\infty^{\alpha\beta}(\boldsymbol{Q}) = -4\pi\rho \frac{Q_\alpha Q_\beta}{Q^2} + \delta_{\alpha,\beta} d_\alpha \quad (9.2.23)$$

where

$$d_\alpha = \frac{4\eta^3}{3\sqrt{\pi}} - 4\pi\rho \sum_{l\neq 0} \frac{(G_l^\alpha)^2}{G_l^2} e^{-\frac{G_l^2}{4\eta^2}} + \frac{2\eta^3}{\sqrt{\pi}} \sum_{l\neq 0} [2(\eta r_l^\alpha)^2 f_D(\eta r_l) - f_B(\eta r_l)]. \quad (9.2.24)$$

Notice that the sum rule

$$d_x + d_y + d_z = 4\pi\rho \quad (9.2.25)$$

can be directly proved using Eq. (9.2.24) and the theta-function transformation (9.2.4). For a SC lattice, one has $d_x = d_y = d_z$ so that the sum rule (9.2.25) gives $d_\alpha = \frac{4}{3}\pi\rho$ and

$$\lim_{\boldsymbol{Q}\to 0} [D_\infty^{\alpha\beta}(\boldsymbol{Q})]_{\mathrm{SC}} = \frac{4\pi}{3a^3} \left(\delta_{\alpha,\beta} - 3\frac{Q_\alpha Q_\beta}{Q^2} \right). \quad (9.2.26)$$

As one can see, for an infinite system Eq. (9.2.23) does not lead to a unique value but to a range of values between $-\frac{8\pi}{3a^3}$ and $\frac{4\pi}{3a^3}$ depending on the direction along which the vector $\boldsymbol{Q}$ tends to zero. All the above results are obtained for an infinite system. Do these conclusions hold when a macroscopic sample of finite volume V is considered? For a finite sample, one has the identity

$$D_V^{\alpha\beta}(\boldsymbol{Q}) = D_\infty^{\alpha\beta}(\boldsymbol{Q}) - D_{\infty-V}^{\alpha\beta}(\boldsymbol{Q}), \quad (9.2.27)$$

where $D_V^{\alpha\beta}(\boldsymbol{Q})$ is the dipolar sum (9.1.7) restricted to the lattice sites contained in the volume V and $D_{\infty-V}^{\alpha\beta}(\boldsymbol{Q})$ is an integral extended to the whole space external to the volume V. The replacement of the discrete sum with an integral is justified by the fact that V is a macroscopic volume so that the sum is expected to be insensitive to the lattice structure since it concerns spins far from the origin. To simplify the calculation of such an integral, let us suppose that the macroscopic sample is a sphere of radius R. In this case, we have

$$D_{\infty-V}^{\alpha\beta}(\boldsymbol{Q}) = \rho \iiint\limits_{r^2>R^2} d^3\boldsymbol{r} \frac{1}{r^3}\left(3\frac{r_\alpha r_\beta}{r^2} - \delta_{\alpha,\beta}\right) e^{i\boldsymbol{Q}\cdot\boldsymbol{r}}. \tag{9.2.28}$$

To perform the calculation of the integral (9.2.28), we choose a new reference system $\xi\eta\zeta$ shown in Fig. 9.1 where the ζ-axis is directed along the vector $\boldsymbol{Q}$ and $r_\xi = r\sin\vartheta\cos\varphi$, $r_\eta = r\sin\vartheta\sin\varphi$, $r_\zeta = r\cos\vartheta$ are the components of the vector $\boldsymbol{r}$ in the new frame. In the $\xi\eta\zeta$ frame one has

$$D_{\infty-V}^{\xi\xi}(0,0,Q) = \rho\int_R^\infty \frac{dr}{r}\int_{-1}^1 d\mu \int_0^{2\pi} d\varphi[3(1-\mu^2)\cos^2\varphi - 1]\, e^{iQr\mu}, \tag{9.2.29}$$

where the change of variable $\mu = \cos\vartheta$ has been done. The integration over φ is direct and one obtains

$$\begin{aligned} D_{\infty-V}^{\xi\xi}(0,0,Q) &= \pi\rho\int_R^\infty \frac{dr}{r}\left[\int_{-1}^1 d\mu e^{iQr\mu} - 3\int_{-1}^1 d\mu\,\mu^2 e^{iQr\mu}\right] \\ &= \pi\rho\int_{QR}^\infty dt\left[-4\frac{\sin t}{t^2} - 12\frac{\cos t}{t^3} + 12\frac{\sin t}{t^4}\right], \end{aligned} \tag{9.2.30}$$

where an integration by parts of the second integral in the first row of Eq. (9.2.30) has been performed and the replacement $t = Qr$ has been done. A further integration by parts of the last two terms of the second row in Eq. (9.2.30) leads to

$$D_{\infty-V}^{\xi\xi}(0,0,Q) = 4\pi\rho f(QR), \tag{9.2.31}$$

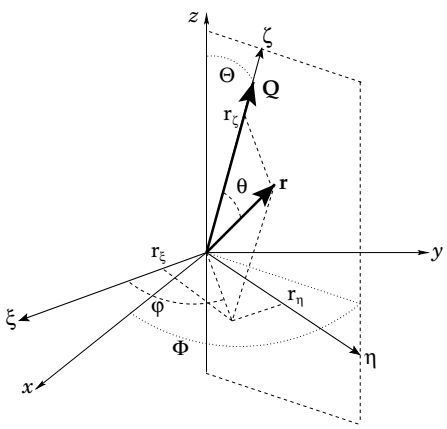

Fig. 9.1. Change of reference frame from (x, y, z) to (ξ, η, ζ) with the ζ-axis chosen parallel to the wavevector $\boldsymbol{Q}$. Θ and Φ are the polar angles of the wavevector $\boldsymbol{Q}$ in the xyz frame; θ and ϕ are the polar angles of the vector $\boldsymbol{r}$ in the $\xi\eta\zeta$ frame.

where

$$f(x) = \frac{\sin x - x\cos x}{x^3}. \tag{9.2.32}$$

In a similar way, one obtains

$$\begin{gathered} D^{\eta\eta}_{\infty-V}(0,0,Q) = D^{\xi\xi}_{\infty-V}(0,0,Q), \quad D^{\zeta\zeta}_{\infty-V}(0,0,Q) = -2D^{\xi\xi}_{\infty-V}(0,0,Q), \\ D^{\xi\eta}_{\infty-V}(0,0,Q) = D^{\xi\zeta}_{\infty-V}(0,0,Q) = D^{\eta\zeta}_{\infty-V}(0,0,Q) = 0. \end{gathered} \tag{9.2.33}$$

Using Eqs. (9.2.33) and the relationship

$$\begin{pmatrix} r_x \\ r_y \\ r_z \end{pmatrix} = \begin{pmatrix} \sin\Phi & \cos\Theta\cos\Phi & \sin\Theta\cos\Phi \\ -\cos\Phi & \cos\Theta\sin\Phi & \sin\Theta\sin\Phi \\ 0 & -\sin\Theta & \cos\Theta \end{pmatrix} \begin{pmatrix} r_\xi \\ r_\eta \\ r_\zeta \end{pmatrix}, \tag{9.2.34}$$

one can write the $D^{\alpha\beta}_{\infty-V}(\boldsymbol{Q})$ with $\alpha,\beta = x,y,z$ given by Eq. (9.2.28) as functions of $D^{\rho\sigma}_{\infty-V}(0,0,Q)$ with $\rho,\sigma = \xi,\eta,\zeta$ given by Eq. (9.2.33). In particular,

$$D^{xx}_{\infty-V}(\boldsymbol{Q}) = (1 - 3\sin^2\Theta\cos^2\Phi) D^{\xi\xi}_{\infty-V}(0,0,Q) \equiv \left(1 - 3\frac{Q_x^2}{Q^2}\right) 4\pi\rho f(QR) \tag{9.2.35}$$

where $f(x)$ is given by Eq. (9.2.32). All the other terms can be obtained in a similar way and the generic term reads

$$D^{\alpha\beta}_{\infty-V}(\boldsymbol{Q}) = \left(\delta_{\alpha,\beta} - 3\frac{Q_\alpha Q_\beta}{Q^2}\right) 4\pi\rho f(QR) \tag{9.2.36}$$

so that

$$D^{\alpha\beta}_{V}(\boldsymbol{Q}) = D^{\alpha\beta}_{\infty}(\boldsymbol{Q}) - \left(\delta_{\alpha,\beta} - 3\frac{Q_\alpha Q_\beta}{Q^2}\right) 4\pi\rho f(QR). \tag{9.2.37}$$

The energy of the ferromagnetic configuration given by Eq. (9.1.10) for a spherical sample of volume V is proportional to

$$D^{\alpha\alpha}_{V}(0) = \lim_{\boldsymbol{Q}\to 0} D^{\alpha\alpha}_{\infty}(\boldsymbol{Q}) - \frac{4\pi}{3}\rho\left(1 - 3\frac{Q_\alpha^2}{Q^2}\right) = d_\alpha - \frac{4\pi}{3}\rho, \tag{9.2.38}$$

where d_α is given by Eq. (9.2.24). The last equality of Eq. (9.2.38) comes from the limit $f(x) \to \frac{1}{3}$ for $x \to 0$. The energy of the antiferromagnetic configuration given by Eq. (9.1.11) for a spherical sample of volume V is proportional to

$$D^{\alpha\alpha}_{V}\left(\frac{\boldsymbol{G}}{2}\right) = D^{\alpha\alpha}_{\infty}\left(\frac{\boldsymbol{G}}{2}\right) \tag{9.2.39}$$

since $f(x) \to 0$ for $x \to \infty$. Note that only for the ferromagnetic configuration, the finiteness of the sample enters a correction to the corresponding value for the infinite system. Moreover, the result for a finite sample has a unique value given by Eq. (9.2.38). For a non-spherical sample, the integral occurring in Eq. (9.2.28) cannot be performed in general. However, for ellipsoidic samples with semi-axis $A \geq B \geq C$ such integral may be expressed in terms of elliptic integrals[84] and the dipolar energy is given by Eq. (9.1.10) with

$$D_V^{\alpha\alpha}(0) = d_\alpha - \rho N_\alpha \tag{9.2.40}$$

where the factors N_α ($\alpha = x, y, z$) are called "demagnetization factors". For a spherical sample, the demagnetization factors are given by $N_x = N_y = N_z = \frac{4\pi}{3}\pi$ so that Eq. (9.2.40) reduce to Eq. (9.2.38). For a "needle" shaped sample[84] ($A \gg B = C$), the demagnetization factors reduce to

$$N_x = 4\pi \left(\frac{C}{A}\right)^2 \left(\ln \frac{2A}{C} - 1\right) + \cdots \to 0 \tag{9.2.41}$$

and

$$N_y = N_z = 4\pi \left[1 - \left(\frac{C}{A}\right)^2 \left(\ln \frac{2A}{C} - 1\right) + \cdots\right] \to 4\pi. \tag{9.2.42}$$

For a "slab" shaped sample[84] ($A = B \gg C$), one obtains

$$N_x = N_y = \pi^2 \frac{C}{A} \left(1 - \frac{4}{\pi}\frac{C}{A} + \cdots\right) \to 0 \tag{9.2.43}$$

and

$$N_z = 4\pi \left(1 - \frac{\pi}{2}\frac{C}{A} + \cdots\right) \to 4\pi. \tag{9.2.44}$$

As one can see from Eqs. (9.2.40)–(9.2.44), the shape of the macroscopic sample determines the orientation of the magnetic moments even in a pure isotropic Heisenberg ferromagnet where the exchange interaction is much greater than the dipolar interaction. For instance, for a SC lattice one has $d_\alpha = \frac{4\pi}{3a^3}$ so that $D_V^{xx}(0) = D_V^{yy}(0) = D_V^{zz}(0) = 0$ for a spherical sample, $D_V^{xx}(0) = \frac{4\pi}{3a^3}$, $D_V^{yy}(0) = D_V^{zz}(0) = -\frac{8\pi}{3a^3}$, for a needle whose axis is directed along the x-axis and $D_V^{xx}(0) = D_V^{yy}(0) = \frac{4\pi}{3a^3}$, $D_V^{zz}(0) = -\frac{8\pi}{3a^3}$ for a slab with the surface parallel to the xy-plane. These values indicate that the magnetic moments may be parallel to any of the three NN directions for a spherical sample; on the contrary, the magnetic moments select the needle-axis direction for a needle-shaped sample and any of the two NN directions (x or y) for a slab-shaped sample. In any case, the continuous symmetry of the isotropic Heisenberg Hamiltonian is broken. Obviously, the previous conclusions can be modified by the presence of an external magnetic field or accounting for the lattice anisotropy (crystalline electric field). In Table 9.1, we give

Table 9.1. Dipolar sums for SC lattice ($a = b = c$). The macroscopic sample is assumed to be a sphere of volume V.

$\boldsymbol{Q} = \frac{2\pi}{a}(q_1, q_2, q_3)$	$a^3 D_V^{xx}(\boldsymbol{Q})$	$a^3 D_V^{yy}(\boldsymbol{Q})$	$a^3 D_V^{zz}(\boldsymbol{Q})$
$(0,0,0)$	0	0	0
$\left(\frac{1}{2},0,0\right)$	−9.6874430	4.8437215	4.8437215
$\left(0,\frac{1}{2},0\right)$	4.8437215	−9.6874430	4.8437215
$\left(0,0,\frac{1}{2}\right)$	4.8437215	4.8437215	−9.6874430
$\left(\frac{1}{2},\frac{1}{2},0\right)$	−2.6767887	−2.6767887	5.3535774
$\left(\frac{1}{2},0,\frac{1}{2}\right)$	−2.6767887	5.3535774	−2.6767887
$\left(0,\frac{1}{2},\frac{1}{2}\right)$	5.3535774	−2.6767887	−2.6767887
$\left(\frac{1}{2},\frac{1}{2},\frac{1}{2}\right)$	0	0	0

the dipolar sums (9.2.38) and (9.2.39) of a SC lattice for a spherical sample: the generic lattice vector $\boldsymbol{r}_l$ is given by

$$\boldsymbol{r}_l = a\,(l_1\mathbf{u}_x + l_2\mathbf{u}_y + l_3\mathbf{u}_z) \tag{9.2.45}$$

and the generic reciprocal lattice vector $\boldsymbol{G}_l$ is given by

$$\boldsymbol{G}_l = \frac{2\pi}{a}(l_1\mathbf{u}_x + l_2\mathbf{u}_y + l_3\mathbf{u}_z). \tag{9.2.46}$$

The numbers given in Table 9.1 are obtained from Eq. (9.2.19) with $-10 < l_1, l_2, l_3 < 10$ and $\eta = \frac{2}{a}$: such numbers do not change within an error of 10^{-10} with increasing l_1, l_2, l_3. No difference between the values for the finite and infinite sample exists for $\boldsymbol{Q} \neq 0$. For $\boldsymbol{Q} = 0$ (first row), the result for the finite sample differs considerably from the result for the infinite system as one can see comparing the values of Table 9.1 with Eq. (9.2.26). Note that a direct evaluation of (9.1.7) summing over the lattice sites within a sphere of radius R leads to values correct within $\frac{1}{(QR)^2}$ so that a sphere containing at least $\sim 10^{15}$ lattice sites is necessary to reach the same precision of the values obtained by the use of the Ewald's method!

From Table 9.1, one can see that the minimum energy configurations corresponding to the maxima of $D^{\alpha\alpha}(\boldsymbol{Q})$ occur for $\boldsymbol{Q} = (\frac{1}{2}, \frac{1}{2}, 0)$ (spins along z), $\boldsymbol{Q} = (\frac{1}{2}, 0, \frac{1}{2})$ (spins along y) and $\boldsymbol{Q} = (0, \frac{1}{2}, \frac{1}{2})$ (spins along x). Neither the ferromagnetic nor the Néel antiferromagnetic phase is supported by the dipolar interaction. The three degenerate ground-state configurations correspond to collinear antiferromagnetic phases in which the spins are directed along the ferromagnetic axis and the ferromagnetic chains are coupled antiferromagnetically to the NN ferromagnetic chains as shown in the upper part of Fig. 9.2. If a tetragonal distortion of the type $c > a = b$

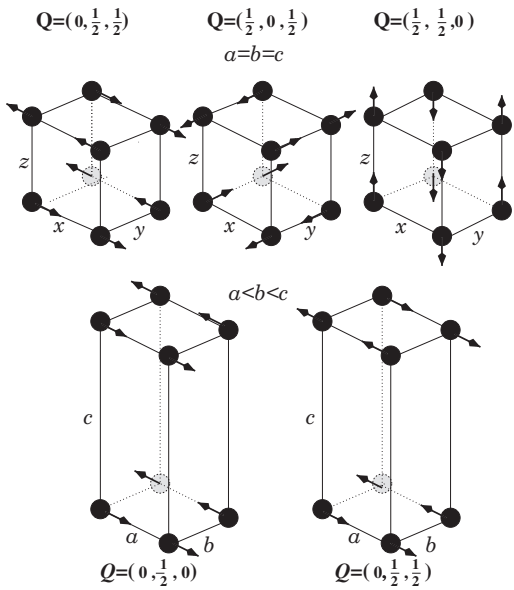

Fig. 9.2. Upper part: degenerate ground-state configurations of a SC lattice with dipole–dipole interactions. Lower part: quasi-degenerate ground-state configurations for an orthorhombic lattice with $b/a = 1.016$ and $c/a = 3.052$.

is entered, the three-fold degenerate ground state of the SC lattice is lifted into a two-fold degenerate ground state whose configurations correspond to $\boldsymbol{Q} = (0, \frac{1}{2}, \frac{1}{2})$ (spins along x) or $\boldsymbol{Q} = (\frac{1}{2}, 0, \frac{1}{2})$ (spins along y). The spin pattern of such configurations is shown in the first two cubes of the upper part of Fig. 9.2. On the contrary, for a tetragonal distortion of the type $c < a = b$, the SC three-fold degenerate ground state reduces to a single ground state corresponding to $\boldsymbol{Q} = (\frac{1}{2}, \frac{1}{2}, 0)$ (spins along z) whose spin pattern is shown in the third cube of the upper part of Fig. 9.2. The common feature of the ground-state configurations of a T lattice is that the spins are directed along the ferromagnetic axis and the NN ferromagnetic chains are coupled antiferromagnetically. An orthorhombic distortion ($a \neq b \neq c$) lifts any degeneracy and the ground-state energy corresponds to a configuration in which the spins are coupled ferromagnetically along the shortest lattice constant. For instance, when $b/a = 1.016$ and $c/a = 3.052$ (the ratios between the lattice constants suitable[79] for $ErBa_2Cu_3O_7$), the ground-state energy corresponds to $\boldsymbol{Q} = (0, \frac{1}{2}, \frac{1}{2})$ (spins along x) and the spin configuration is shown in the second parallelepiped of the lower part of Fig. 9.2.

9.3. Ground-State Configuration of $ErBa_2Cu_3O_{6+x}$

The aim of this section is to show how the experimental data on $ErBa_2Cu_3O_{6+x}$ can be used to select among the theoretical models of the previous section in order to check the experiment. Evaluating the dipolar sums given by Eqs. (9.2.38) and

Table 9.2. Dipolar sums for $b/a = 1.016$ and $c/a = 3.052$ (orthorhombic symmetry): these are the lattice space ratios of[79] $ErBa_2Cu_3O_7$.

$\boldsymbol{Q} = \frac{2\pi}{a}(q_1, q_2, q_3)$	$a^3 D_V^{xx}(\boldsymbol{Q})$	$a^3 D_V^{yy}(\boldsymbol{Q})$	$a^3 D_V^{zz}(\boldsymbol{Q})$
$(0,0,0)$	3.1960006	2.9244265	−6.1204271
$\left(\frac{1}{2},0,0\right)$	−5.8977753	4.8930604	1.0047149
$\left(0,\frac{1}{2},0\right)$	5.0689676	−5.9018694	0.8329018
$\left(0,0,\frac{1}{2}\right)$	4.5468622	4.2752885	−8.8221507
$\left(\frac{1}{2},\frac{1}{2},0\right)$	−1.4501090	−1.1350864	2.5851954
$\left(\frac{1}{2},0,\frac{1}{2}\right)$	−5.8871227	4.8930607	0.9940620
$\left(0,\frac{1}{2},\frac{1}{2}\right)$	5.0689679	−5.8896758	0.8207079
$\left(\frac{1}{2},\frac{1}{2},\frac{1}{2}\right)$	−1.4497908	−1.1347781	2.5845688

Table 9.3. Dipolar sums for $b/a = 1$ (tetragonal symmetry) and $c/a = 3.062$: these are the lattice space ratios of[80] $ErBa_2Cu_3O_6$.

$\boldsymbol{Q} = \frac{2\pi}{a}(q_1, q_2, q_3)$	$a^3 D_V^{xx}(\boldsymbol{Q})$	$a^3 D_V^{yy}(\boldsymbol{Q})$	$a^3 D_V^{zz}(\boldsymbol{Q})$
$(0,0,0)$	3.1488185	3.1488185	−6.2976372
$\left(\frac{1}{2},0,0\right)$	−6.0395796	5.0988729	0.9407067
$\left(0,\frac{1}{2},0\right)$	5.0988729	−6.0395796	0.9407067
$\left(0,0,\frac{1}{2}\right)$	4.5168115	4.5168115	−9.0336231
$\left(\frac{1}{2},\frac{1}{2},0\right)$	−1.3230812	−1.3230812	2.6461624
$\left(\frac{1}{2},0,\frac{1}{2}\right)$	−6.0290914	5.0988731	0.9302183
$\left(0,\frac{1}{2},\frac{1}{2}\right)$	5.0988731	−6.0290914	0.9302183
$\left(\frac{1}{2},\frac{1}{2},\frac{1}{2}\right)$	−1.3228053	−1.3228053	2.6456106

(9.2.39) for an orthorhombic lattice with the lattice constants of the oxygenate compound[79] ($x = 1$) and for a tetragonal lattice with the lattice constants of the deoxygenated compound[80] ($x \simeq 0$), we obtain Tables 9.2 and 9.3, respectively. The dipolar energy is given by

$$E_{\rm dip}^{\alpha}(\boldsymbol{Q}) = -\frac{(g\mu_B S)^2}{2} N D_V^{\alpha\alpha}(\boldsymbol{Q}). \tag{9.3.1}$$

The Bohr magneton μ_B occurring in Eq. (9.3.1) is given by

$$\mu_B = \frac{e\hbar}{2m_e c} = 9.27401 \times 10^{-21}\,\mathrm{erg}^{\frac{1}{2}}\mathrm{cm}^{\frac{3}{2}} \tag{9.3.2}$$

where $e = 4.8032 \times 10^{-10}$ stat C is the absolute value of the electron charge (1 stat $\mathrm{C} = 1\ \mathrm{erg}^{\frac{1}{2}}\mathrm{cm}^{\frac{1}{2}}$ from the Coulomb law in the CGS system), $\hbar = 1.05457 \times 10^{-27}$ erg $\times$ s is the reduced Planck's constant, $m_e = 9.10938 \times 10^{-28}$ g is the electron mass and $c = 2.99792 \times 10^{10}$ cm/s is the light speed. Using Eq. (9.3.2), one sees that the dipolar energy (9.3.1) measured in units of Boltzmann constant $k_B = 1.38065 \times 10^{-16}$ erg/K becomes

$$\frac{E^{\alpha}_{\mathrm{dip}}(\boldsymbol{Q})}{k_B N} = -0.62295\frac{(gS)^2}{2} D_V^{\alpha\alpha}(\boldsymbol{Q}) \quad (\mathrm{K\AA}^3). \tag{9.3.3}$$

For[79] $gS \simeq 4.9$ and $a = 3.82$ Å, Eq. (9.3.3) gives

$$\frac{E^{\alpha}_{\mathrm{dip}}(\boldsymbol{Q})}{k_B N} = -0.1342\,[a^3 D_V^{\alpha\alpha}(\boldsymbol{Q})] \quad (\mathrm{K}), \tag{9.3.4}$$

where $a^3 D_V^{\alpha\alpha}(\boldsymbol{Q})$ are given in Table 9.2 from which one can see that the ground-state energy corresponds to $D_V^{xx}(0, \frac{1}{2}, \frac{1}{2}) = 5.0689679/a^3$ even though the configuration corresponding to $D_V^{xx}(0, \frac{1}{2}, 0) = 5.0689676/a^3$ is very close in energy. The spin patterns of these two configurations are shown in the lower part of Fig. 9.2. In the ground-state configuration, the spins are aligned along the ferromagnetic a-axis and the ferromagnetic chains are coupled antiferromagnetically both along the b and c-axes. In the quasi-degenerate configuration, the ferromagnetic chains are coupled ferromagnetically along the c-axis. The close energy values of the two configurations are explained by the very weak dipole–dipole coupling of the Er^{3+} ions along the c-axis due to the large spacing $c \sim 3a$.

From Table 9.3, one can see that the ground state of the tetragonal $ErBa_2Cu_3O_6$ is degenerate corresponding to the two configurations $D_V^{xx}(0, \frac{1}{2}, \frac{1}{2})$ $= D_V^{yy}(\frac{1}{2}, 0, \frac{1}{2}) = 5.0988731/a^3$ with the spins directed along the ferromagnetic axis. Other two degenerate configurations corresponding to $D_V^{xx}(0, \frac{1}{2}, 0) = D_V^{yy}(\frac{1}{2}, 0, 0)$ $= 5.0988729/a^3$ with the spins directed along the shortest ferromagnetic axis are very close in energy.

In a neutron scattering experiment,[79] both elastic Bragg peaks at $(\frac{1}{2}, 0, 0)$ and $(\frac{1}{2}, 0, \frac{1}{2})$ have been recorded for the orthorhombic $ErBa_2Cu_3O_7$ with the spins directed along the ferromagnetic b-axis. This contrasts with the values of the dipolar sums given in Table 9.2 where the configurations corresponding to the experiment are given by $D_V^{yy}(\frac{1}{2}, 0, 0) = 4.8930604/a^3$ and $D_V^{yy}(\frac{1}{2}, 0, \frac{1}{2}) = 4.8930607/a^3$, while the two lowest energies of the theoretical model correspond to $D_V^{xx}(0, \frac{1}{2}, \frac{1}{2}) =$ $5.0689679/a^3$ and $D_V^{xx}(0, \frac{1}{2}, 0) = 5.0689676/a^3$ with the spins aligned along the a-axis as shown in the lower part of Fig. 9.2. As for the tetragonal $ErBa_2Cu_3O_6$, no elastic Bragg peaks were recorded since the LRO is absent.

How to reconcile the theory with the experiment for the orthorhombic compound? In other words, which important features of the actual compound have been lost in the theoretical model? The theoretical model certainly neglects any

antiferromagnetic exchange coupling between the NN erbium ions belonging to NN chains. However, it is expected that such interaction is very weak due to the indirect exchange through the bridges over the oxygen and copper ions. More importantly, such antiferromagnetic interaction should favour a Néel antiferromagnetic order in contrast to that observed in the experiment. The theoretical model also neglects any interaction between the Er^{3+} ions and its surrounding oxygen or copper ions. The simplest way to account for such an interaction is to introduce the electrostatic potential between the electrons of the unfilled shell $4f$ of the Er^{3+} ion and the surrounding oxygen ions represented as point-charges. This model is called the point-charge model[85] and the electrostatic potential is called the crystalline-electric-field (CEF) potential.

9.4. CEF Calculation for $ErBa_2Cu_3O_{6+x}$

In this section, we give a sketch of the CEF calculation[80] for $ErBa_2Cu_3O_{6+x}$. The eight NN oxygen ions are located on the vertices of a parallelepiped with edges $2a, 2b, 2c$ which do not coincide with the lattice constants of the orthorhombic lattice of the Er^{3+} ions. The erbium ion location at the centre of the parallelepiped is assumed to be the origin of the reference coordinate system as shown in Fig. 9.3. Assuming that the oxygen ions behave like point-charges q, the crystalline field potential at a point $\boldsymbol{r} = (x, y, z)$ near the origin is given by[85]

$$V_{\mathrm{CEF}}(\boldsymbol{r}) = \sum_{i=1}^{8} \frac{q}{|\boldsymbol{r} - \boldsymbol{R}_i|} = \sum_{s=0}^{\infty} \frac{4\pi q}{2s+1} \frac{r^s}{R^{s+1}} \sum_{m=-s}^{s} A_s^{-m} Y_s^m \left(\frac{\boldsymbol{r}}{r}\right) \tag{9.4.1}$$

with $\boldsymbol{R}_i = (\pm a, \pm b, \pm c)$, $R = \sqrt{a^2 + b^2 + c^2}$ is the distance of each oxygen ion from the origin and

$$A_s^m = \sum_{i=1}^{8} (-1)^m Y_s^m \left(\frac{\boldsymbol{R}_i}{R}\right). \tag{9.4.2}$$

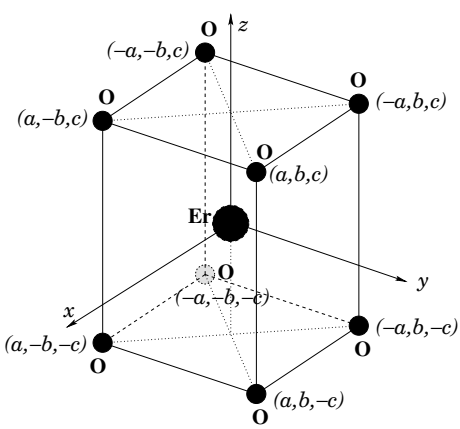

Fig. 9.3. Parallelepiped of oxygen ions O surrounding the Er^{3+} ion.

The spherical harmonics expansion given in Eq. (9.4.1) is known as the "spherical harmonics addition theorem". Such an expansion consists of infinite terms each of which is a product of two spherical harmonics, one having as argument the polar angles of the vector $\boldsymbol{r}$ and the other one the polar angles of the vertices of the parallelepiped, that is, the coordinates of the oxygen point-charges. This model is referred as point-charge model.[85] The spherical harmonics written as a function of the cartesian coordinates instead of the polar angles are

$$Y_0^0 = \frac{1}{\sqrt{4\pi}}, \tag{9.4.3}$$

$$Y_1^0 = \frac{1}{2}\sqrt{\frac{3}{\pi}}\,\frac{z}{r}, \quad Y_1^{\mp 1} = \pm\frac{1}{2}\sqrt{\frac{3}{2\pi}}\,\frac{(x \mp iy)}{r}, \tag{9.4.4}$$

$$Y_2^0 = \frac{1}{4}\sqrt{\frac{5}{\pi}}\,\frac{(3z^2 - r^2)}{r^2}, \quad Y_2^{\mp 1} = \pm\frac{1}{2}\sqrt{\frac{15}{2\pi}}\,\frac{(x \mp iy)z}{r^2}, \quad Y_2^{\mp 2} = \frac{1}{4}\sqrt{\frac{15}{2\pi}}\,\frac{(x \mp iy)^2}{r^2}, \tag{9.4.5}$$

$$\begin{aligned} Y_3^0 &= \frac{1}{4}\sqrt{\frac{7}{\pi}}\,\frac{(5z^2 - 3r^2)z}{r^3}, \quad Y_3^{\mp 1} = \pm\frac{1}{8}\sqrt{\frac{21}{\pi}}\,\frac{(x \mp iy)(5z^2 - r^2)}{r^3}, \\ Y_3^{\mp 2} &= \frac{1}{4}\sqrt{\frac{105}{2\pi}}\,\frac{(x \mp iy)^2 z}{r^3}, \quad Y_3^{\mp 3} = \pm\frac{1}{8}\sqrt{\frac{35}{\pi}}\,\frac{(x \mp iy)^3}{r^3}, \end{aligned} \tag{9.4.6}$$

$$\begin{aligned} Y_4^0 &= \frac{3}{16}\sqrt{\frac{1}{\pi}}\,\frac{(35z^4 - 30z^2r^2 + 3r^4)}{r^4}, \quad Y_4^{\mp 1} = \pm\frac{3}{8}\sqrt{\frac{5}{\pi}}\,\frac{(x \mp iy)z(7z^2 - 3r^2)}{r^4}, \\ Y_4^{\mp 2} &= \frac{3}{8}\sqrt{\frac{5}{2\pi}}\,\frac{(x \mp iy)^2(7z^2 - r^2)}{r^4}, \quad Y_4^{\mp 3} = \pm\frac{3}{8}\sqrt{\frac{35}{\pi}}\,\frac{(x \mp iy)^3 z}{r^4}, \\ Y_4^{\mp 4} &= \frac{3}{16}\sqrt{\frac{35}{2\pi}}\,\frac{(x \mp iy)^4}{r^4}, \end{aligned} \tag{9.4.7}$$

$$\begin{aligned} Y_5^0 &= \frac{1}{16}\sqrt{\frac{11}{\pi}}\,\frac{(63z^4 - 70z^2r^2 + 15r^4)z}{r^5}, \\ Y_5^{\mp 1} &= \pm\frac{1}{16}\sqrt{\frac{165}{2\pi}}\,\frac{(x \mp iy)(21z^4 - 14z^2r^2 + r^4)}{r^5}, \\ Y_5^{\mp 2} &= \frac{1}{8}\sqrt{\frac{1155}{2\pi}}\,\frac{(x \mp iy)^2 z(3z^2 - r^2)}{r^5}, \quad Y_5^{\mp 3} = \pm\frac{1}{32}\sqrt{\frac{385}{\pi}}\,\frac{(x \mp iy)^3(9z^2 - r^2)}{r^5}, \\ Y_5^{\mp 4} &= \frac{3}{16}\sqrt{\frac{385}{2\pi}}\,\frac{(x \mp iy)^4 z}{r^5}, \quad Y_5^{\mp 5} = \pm\frac{3}{32}\sqrt{\frac{77}{\pi}}\,\frac{(x \mp iy)^5}{r^5}, \end{aligned} \tag{9.4.8}$$

$$\begin{aligned} Y_6^0 &= \frac{1}{32}\sqrt{\frac{13}{\pi}}\,\frac{(231z^6 - 315z^4r^2 + 105z^2r^4 - 5r^6)}{r^6}, \\ Y_6^{\mp 1} &= \pm\frac{1}{16}\sqrt{\frac{273}{2\pi}}\,\frac{(x \mp iy)z(33z^4 - 30z^2r^2 + 5r^4)}{r^6}, \end{aligned}$$

$$Y_6^{\mp 2} = \frac{1}{64}\sqrt{\frac{1365}{\pi}}\frac{(x \mp iy)^2(33z^4 - 18z^2r^2 + r^4)}{r^6},$$
$$Y_6^{\mp 3} = \pm\frac{1}{32}\sqrt{\frac{1365}{\pi}}\frac{(x \mp iy)^3 z(11z^2 - 3r^2)}{r^6}, \quad Y_6^{\mp 4} = \frac{3}{32}\sqrt{\frac{91}{2\pi}}\frac{(x \mp iy)^4(11z^2 - r^2)}{r^6},$$
$$Y_6^{\mp 5} = \pm\frac{3}{32}\sqrt{\frac{1001}{\pi}}\frac{(x \mp iy)^5 z}{r^6}, \quad Y_6^{\mp 6} = \frac{1}{64}\sqrt{\frac{3003}{\pi}}\frac{(x \mp iy)^6}{r^6}. \tag{9.4.9}$$

Note that the sum in Eq. (9.4.2) can be performed easily using the spherical harmonics (9.4.3)–(9.4.9) evaluated at the points $\mathbf{R}_i = (\pm a, \pm b, \pm c)$. It is direct to see that due to the orthorhombic symmetry of the surrounding oxygen ions and to the nature of the spherical harmonics the only terms A_s^m that give non-zero contribution are those with both s and m even. Then from Eq. (9.4.2), one obtains

$$A_0^0 = \frac{8}{\sqrt{4\pi}}, \tag{9.4.10}$$
$$A_2^0 = \frac{2}{R^2}\sqrt{\frac{5}{\pi}}(3c^2 - R^2), \tag{9.4.11}$$
$$A_2^{\pm 2} = \frac{2}{R^2}\sqrt{\frac{15}{2\pi}}(a^2 - b^2), \tag{9.4.12}$$
$$A_4^0 = \frac{3}{2R^4}\sqrt{\frac{1}{\pi}}(35c^4 - 30c^2R^2 + 3R^4), \tag{9.4.13}$$
$$A_4^{\pm 2} = \frac{3}{R^4}\sqrt{\frac{5}{2\pi}}(a^2 - b^2)(7c^2 - R^2), \tag{9.4.14}$$
$$A_4^{\pm 4} = \frac{3}{2R^4}\sqrt{\frac{35}{2\pi}}(a^4 - 6a^2b^2 + b^4), \tag{9.4.15}$$
$$A_6^0 = \frac{1}{4R^6}\sqrt{\frac{13}{\pi}}(231c^6 - 315c^4R^2 + 105c^2R^4 - 5R^6), \tag{9.4.16}$$
$$A_6^{\pm 2} = \frac{1}{8R^6}\sqrt{\frac{1365}{\pi}}(a^2 - b^2)(33c^4 - 18c^2R^2 + R^4), \tag{9.4.17}$$
$$A_6^{\pm 4} = \frac{3}{4R^6}\sqrt{\frac{91}{2\pi}}(a^4 - 6a^2b^2 + b^4)(11c^2 - R^2) \tag{9.4.18}$$

and

$$A_6^{\pm 6} = \frac{1}{8R^6}\sqrt{\frac{3003}{\pi}}(a^2 - b^2)(a^4 - 14a^2b^2 + b^4). \tag{9.4.19}$$

From Eqs. (9.4.1) and (9.4.10)–(9.4.19), one obtains the CEF potential. Then the CEF Hamiltonian is obtained multiplying the potential by the electron charge

$-e$ ($e = 4.8032 \times 10^{-10}$ stat C) and summing over the 11 electrons of the unfilled $4f$-shell of the Er^{3+} ion. One obtains

$$\begin{aligned}\mathcal{H}_{\rm CEF} = &-\sum_i \frac{8eq}{R} - \frac{4\pi eq}{5R^3}\sum_i r_i^2\,[A_2^0 Y_2^0 + A_2^2(Y_2^2 + Y_2^{-2})] \\ &- \frac{4\pi eq}{9R^5}\sum_i r_i^4\,[A_4^0 Y_4^0 + A_4^2\,(Y_4^2 + Y_4^{-2}) + A_4^4\,(Y_4^4 + Y_4^{-4})] \\ &- \frac{4\pi eq}{13R^7}\sum_i r_i^6\,[A_6^0 Y_6^0 + A_6^2\,(Y_6^2 + Y_6^{-2}) \\ &+ A_6^4\,(Y_6^4 + Y_6^{-4}) + A_6^6\,(Y_6^6 + Y_6^{-6})], \end{aligned} \tag{9.4.20}$$

where the arguments of the spherical harmonics, omitted in Eq. (9.4.20), are the angular coordinates (θ_i, ϕ_i) of the electrons. The free ion Er^{3+} has an electronic configuration $(Xe)4f^{11}$ where Xe means the electronic configuration of the noble gas xenon. The spin and orbital quantum numbers of the ground-state multiplet are $S = \frac{3}{2}$ and $L = 6$, respectively. The total angular momentum is given by the Hund's rule $J = L + S = \frac{15}{2}$ so that the ground-state multiplet of the free Er^{3+} ion is $|L = 6, S = \frac{3}{2}; J = \frac{15}{2}, M\rangle$ ($^4I_{15/2}$) with $M = -\frac{15}{2}, \ldots, \frac{15}{2}$ (16-fold degenerate). The first excited multiplet ($^4I_{13/2}$) has an energy 0.8 eV higher. Since the overall CEF splitting is of the order of $\sim$0.1 eV in a first approximation, one can neglect any mixing between different J multiplets and one can use the first-order perturbation theory applied to the degenerate ground-state multiplet. Moreover, for electrons $4f$ the infinite terms of Hamiltonian (9.4.1) are reduced to the finite number of terms given in Eq. (9.4.20). Indeed, the matrix elements of the CEF Hamiltonian between the unperturbed states $|L = 6, S = \frac{3}{2}; J = \frac{15}{2}, M\rangle$ are combinations of Slater's determinants which are combinations of direct products of one-electron states $|\Psi_{nlm\sigma}\rangle = R_n(r)Y_l^m(\theta,\phi)\chi_\sigma$ where $n = 4$, $l = 3, m = -3, \ldots, 3$ and $\sigma = \pm\frac{1}{2}$. Then the matrix elements of the CEF Hamiltonian (9.4.20) $\langle\Psi_{4fm''\sigma''}|\mathcal{H}_{\rm CEF}|\Psi_{4fm'\sigma'}\rangle$ involve integrals like

$$(-1)^{m''}\delta_{\sigma',\sigma''}\langle r^s\rangle \int_0^\pi \sin\theta\, d\theta \int_0^{2\pi} d\phi Y_3^{-m''}(\theta,\phi) A_s^m Y_s^m(\theta,\phi) Y_3^{m'}(\theta,\phi), \tag{9.4.21}$$

where

$$\langle r^s\rangle = \int_0^\infty r^2 dr\, r^s R_4(r)^2 \tag{9.4.22}$$

with $m', m'' = -3, \ldots, 3$. The simultaneous occurrence of three spherical harmonics in the integral of Eq. (9.4.21) implies that it is not zero only if $s \leq 6$ with s an even integer and $|m'' - m'| = m$. In principle, one can obtain the matrix elements directly from Eq. (9.4.21) keeping the radial part (9.4.22) as a parameter since the radial function $R_4(r)$ of the free ion is not accurately known.

However, a much more convenient method of obtaining equivalent results is to replace the sums over the electron coordinates in Eq. (9.4.20) by the "Stevens' operator equivalents" in such a way that the matrix elements of the CEF Hamiltonian

written in terms of the angular momentum operators J_+, J_-, J_z between the states $|L, S; J, M\rangle$ are the same as the matrix elements of the original CEF Hamiltonian (9.4.20) between the same eigenfunctions. The correspondence between the sums over the eleven $4f$ electrons and the Stevens' operator equivalents is given by[85]

$$\sum_i r_i^2 Y_2^0\left(\frac{\boldsymbol{r}_i}{r_i}\right) = \frac{1}{4}\sqrt{\frac{5}{\pi}}\alpha_J\langle r^2\rangle O_2^0, \tag{9.4.23}$$

$$\sum_i r_i^2\left[Y_2^2\left(\frac{\boldsymbol{r}_i}{r_i}\right) + Y_2^{-2}\left(\frac{\boldsymbol{r}_i}{r_i}\right)\right] = \frac{1}{2}\sqrt{\frac{15}{2\pi}}\alpha_J\langle r^2\rangle O_2^2, \tag{9.4.24}$$

$$\sum_i r_i^4 Y_4^0\left(\frac{\boldsymbol{r}_i}{r_i}\right) = \frac{3}{16}\sqrt{\frac{1}{\pi}}\beta_J\langle r^4\rangle O_4^0, \tag{9.4.25}$$

$$\sum_i r_i^4\left[Y_4^2\left(\frac{\boldsymbol{r}_i}{r_i}\right) + Y_4^{-2}\left(\frac{\boldsymbol{r}_i}{r_i}\right)\right] = \frac{3}{4}\sqrt{\frac{5}{2\pi}}\beta_J\langle r^4\rangle O_4^2, \tag{9.4.26}$$

$$\sum_i r_i^4\left[Y_4^4\left(\frac{\boldsymbol{r}_i}{r_i}\right) + Y_4^{-4}\left(\frac{\boldsymbol{r}_i}{r_i}\right)\right] = \frac{3}{8}\sqrt{\frac{35}{2\pi}}\beta_J\langle r^4\rangle O_4^4, \tag{9.4.27}$$

$$\sum_i r_i^6 Y_6^0\left(\frac{\boldsymbol{r}_i}{r_i}\right) = \frac{1}{32}\sqrt{\frac{13}{\pi}}\gamma_J\langle r^6\rangle O_6^0, \tag{9.4.28}$$

$$\sum_i r_i^6\left[Y_6^2\left(\frac{\boldsymbol{r}_i}{r_i}\right) + Y_6^{-2}\left(\frac{\boldsymbol{r}_i}{r_i}\right)\right] = \frac{1}{32}\sqrt{\frac{1365}{\pi}}\gamma_J\langle r^6\rangle O_6^2, \tag{9.4.29}$$

$$\sum_i r_i^6\left[Y_6^4\left(\frac{\boldsymbol{r}_i}{r_i}\right) + Y_6^{-4}\left(\frac{\boldsymbol{r}_i}{r_i}\right)\right] = \frac{3}{16}\sqrt{\frac{91}{2\pi}}\gamma_J\langle r^6\rangle O_6^4 \tag{9.4.30}$$

and

$$\sum_i r_i^6\left[Y_6^6\left(\frac{\boldsymbol{r}_i}{r_i}\right) + Y_6^{-6}\left(\frac{\boldsymbol{r}_i}{r_i}\right)\right] = \frac{1}{32}\sqrt{\frac{3003}{\pi}}\gamma_J\langle r^6\rangle O_6^6, \tag{9.4.31}$$

where[85] $\alpha_J = \frac{4}{1575}$, $\beta_J = \frac{2}{45045}$ and $\gamma_J = \frac{8}{3864861}$ for Er^{3+}. For $J = \frac{15}{2}$, the Stevens' operator equivalents O_n^m occurring in (9.4.23)–(9.4.31) are given by[85]

$$O_2^0 = 3J_z^2 - \frac{255}{4}, \tag{9.4.32}$$

$$O_4^0 = 35J_z^4 - \frac{3775}{2}J_z^2 + \frac{188955}{16}, \tag{9.4.33}$$

$$O_6^0 = 231J_z^6 - \frac{77385}{4}J_z^4 + \frac{6296829}{16}J_z^2 - \frac{72747675}{64}, \tag{9.4.34}$$

$$O_2^2 = \frac{1}{2}(J_+^2 + J_-^2), \tag{9.4.35}$$

$$O_4^2 = \frac{1}{4}\left[\left(7J_z^2 - \frac{275}{4}\right)(J_+^2 + J_-^2) + (J_+^2 + J_-^2)\left(7J_z^2 - \frac{275}{4}\right)\right], \tag{9.4.36}$$

$$O_6^2 = \frac{1}{4}\left[\left(33\,J_z^4 - \frac{2541}{2}J_z^2 + \frac{76857}{16}\right)(J_+^2 + J_-^2) + (J_+^2 + J_-^2)\left(33\,J_z^4 - \frac{2541}{2}J_z^2 + \frac{76857}{16}\right)\right], \tag{9.4.37}$$

$$O_4^4 = \frac{1}{2}(J_+^4 + J_-^4), \tag{9.4.38}$$

$$O_6^4 = \frac{1}{4}\left[\left(11\,J_z^2 - \frac{407}{4}\right)(J_+^4 + J_-^4) + (J_+^4 + J_-^4)\left(11\,J_z^2 - \frac{407}{4}\right)\right], \tag{9.4.39}$$

$$O_6^6 = \frac{1}{2}(J_+^6 + J_-^6) \tag{9.4.40}$$

and the CEF Hamiltonian (9.4.20) becomes[80]

$$\mathcal{H}_{\rm CEF} = B_2^0 O_2^0 + B_4^0 O_4^0 + B_6^0 O_6^0 + B_2^2 O_2^2 + B_4^2 O_4^2 + B_6^2 O_6^2 + B_4^4 O_4^4 + B_6^4 O_6^4 + B_6^6 O_6^6. \tag{9.4.41}$$

In Eq. (9.4.41), we have ignored the constant term of Eq. (9.4.20). Moreover, the coefficients B_n^m occurring in Eq. (9.4.41) are proportional to the coefficients A_n^m appearing in Eq. (9.4.20) through the averages $\langle r^2\rangle, \langle r^4\rangle$ and $\langle r^6\rangle$ which are not known. So the parameters B_n^m have to be determined by a fitting with the experiment.[80] Indeed, the matrix elements of the CEF Hamiltonian (9.4.41)

$$\langle M|\mathcal{H}_{\rm CEF}|M'\rangle, \quad M, M' = \frac{15}{2}, \frac{13}{2}, \ldots, -\frac{13}{2}, -\frac{15}{2} \tag{9.4.42}$$

are evaluated using the matrix elements of the angular momentum operators O_n^m. The diagonal elements are given in Table 9.4. The non-zero off-diagonal terms of the

Table 9.4. Matrix elements of the diagonal Stevens' operator equivalents for $J = \frac{15}{2}$.

M	$\frac{1}{3}\langle M\|O_2^0\|M\rangle$	$\frac{1}{60}\langle M\|O_4^0\|M\rangle$	$\frac{1}{13860}\langle M\|O_6^0\|M\rangle$
$\pm\frac{15}{2}$	35	273	65
$\pm\frac{13}{2}$	21	−91	−117
$\pm\frac{11}{2}$	9	−221	−39
$\pm\frac{9}{2}$	−1	−201	59
$\pm\frac{7}{2}$	−9	−101	87
$\pm\frac{5}{2}$	−15	23	45
$\pm\frac{3}{2}$	−19	129	−25
$\pm\frac{1}{2}$	−21	189	−75

Table 9.5. Matrix elements of the off-diagonal Stevens' operator equivalents for $J = \frac{15}{2}$.

M	$\langle \pm M\|O_2^2\| \pm (M-2)\rangle$	$\frac{1}{6}\langle \pm M\|O_4^2\| \pm (M-2)\rangle$	$\frac{1}{1320}\langle \pm M\|O_6^2\| \pm (M-2)\rangle$
$\frac{15}{2}$	$\sqrt{105}$	$39\sqrt{105}$	$13\sqrt{105}$
$\frac{13}{2}$	$\sqrt{273}$	$25\sqrt{273}$	$\sqrt{273}$
$\frac{11}{2}$	$6\sqrt{13}$	$80\sqrt{13}$	$-21\sqrt{13}$
$\frac{9}{2}$	$2\sqrt{165}$	$8\sqrt{165}$	$-7\sqrt{165}$
$\frac{7}{2}$	$5\sqrt{33}$	$-15\sqrt{33}$	$-7\sqrt{33}$
$\frac{5}{2}$	$3\sqrt{105}$	$-23\sqrt{105}$	$3\sqrt{105}$
$\frac{3}{2}$	$12\sqrt{7}$	$-120\sqrt{7}$	$30\sqrt{7}$

Table 9.6. Matrix elements of the off-diagonal Stevens' operator equivalents for $J = \frac{15}{2}$.

M	$\frac{1}{12}\langle \pm M\|O_4^4\| \pm (M-4)\rangle$	$\frac{1}{660}\langle \pm M\|O_4^6\| \pm (M-4)\rangle$	$\frac{1}{360\sqrt{11}}\langle \pm M\|O_6^6\| \pm (M-6)\rangle$
$\frac{15}{2}$	$\sqrt{1365}$	$5\sqrt{1365}$	$\sqrt{455}$
$\frac{13}{2}$	$\sqrt{5005}$	$3\sqrt{5005}$	$7\sqrt{39}$
$\frac{11}{2}$	$5\sqrt{429}$	$7\sqrt{429}$	$4\sqrt{273}$
$\frac{9}{2}$	$15\sqrt{77}$	$3\sqrt{77}$	84
$\frac{7}{2}$	$10\sqrt{231}$	$-6\sqrt{231}$	$42\sqrt{5}$
$\frac{5}{2}$	$42\sqrt{15}$	$-42\sqrt{15}$	0

CEF Hamiltonian are obtained from Tables 9.5 and 9.6. These tables reflect the properties of the raising and lowering angular momentum operators $J_\pm$. Indeed, the only non-zero terms of O_n^2 with $n = 2, 4, 6$ are those in which M changes of ± 2 since they contain $J_\pm^2$ operators. Similarly, the only non-zero matrix elements of the operators O_n^4 with $n = 4, 6$ and O_6^6 are those in which M changes of ± 4 and ± 6, respectively. Note that the same matrix elements are obtained from the hermitian conjugate terms of CEF Hamiltonian since $(O_n^m)^+ = O_n^m$ so that the 16×16 matrix (9.4.42) is symmetric with respect to its main diagonal. The hermiticity of the CEF Hamiltonian assures that its eigenvalues are real. Using Tables 9.4–9.6 one can write all the elements of the CEF matrix for the ground-state multiplet. One can see that the CEF matrix is also symmetric with respect to its second diagonal, implying that

all its eigenvalues are doubly degenerate. Obviously, this symmetry is broken by the introduction of an external magnetic field. The eigenvalues of the matrix (9.4.42) are functions of the parameters B_n^m that are determined by fitting the differences between the matrix eigenvalues with the transition energies obtained from the INS. The best fit for $ErBa_2Cu_3O_7$ leads to the following values[80] of the B_n^m (in meV)

$$\begin{aligned} &B_2^0 = 3.54 \times 10^{-2}, \quad B_4^0 = -1.43 \times 10^{-3}, \quad B_6^0 = 7.6 \times 10^{-6}, \\ &B_2^2 = 2.96 \times 10^{-2}, \quad B_4^2 = 4.56 \times 10^{-4}, \quad B_6^2 = -1.18 \times 10^{-6}, \\ &B_4^4 = 6.96 \times 10^{-3}, \quad B_6^4 = 2.16 \times 10^{-4}, \quad B_6^6 = 1.33 \times 10^{-6}. \end{aligned} \tag{9.4.43}$$

From the choice of parameters given in (9.4.43), one obtains the eigenvalues

$$\begin{aligned} E_1 = E_2 &= -41.33\,\text{meV} \Rightarrow E_{1,2}/k_B = 0\,\text{K}, \\ E_3 = E_4 &= -31.10\,\text{meV} \Rightarrow E_{3,4}/k_B = 119\,\text{K}, \\ E_5 = E_6 &= -30.46\,\text{meV} \Rightarrow E_{5,6}/k_B = 126\,\text{K}, \\ E_7 = E_8 &= -29.37\,\text{meV} \Rightarrow E_{7,8}/k_B = 139\,\text{K}, \\ E_9 = E_{10} &= 26.88\,\text{meV} \Rightarrow E_{9,10}/k_B = 792\,\text{K}, \\ E_{11} = E_{12} &= 30.74\,\text{meV} \Rightarrow E_{11,12}/k_B = 836\,\text{K}, \\ E_{13} = E_{14} &= 35.45\,\text{meV} \Rightarrow E_{13,14}/k_B = 891\,\text{K}, \\ E_{15} = E_{16} &= 39.19\,\text{meV} \Rightarrow E_{15,16}/k_B = 935\,\text{K}, \end{aligned} \tag{9.4.44}$$

where the last values of the energy levels are expressed in Kelvin degrees assuming the lowest energy doublet as the zero of the energy scale. The generic eigenvector belonging to the eigenvalue E_n is given by

$$|\psi_n\rangle = \sum_{M=-15/2}^{M=15/2} a_M^n |M\rangle, \tag{9.4.45}$$

where the coefficients a_M^n can be univocally determined using the normalization condition and breaking the symmetry of the CEF Hamiltonian entering an infinitesimal magnetic field directed along the z-axis. The infinitesimal magnetic field does not change the eigenvalues but eliminates the arbitrariness in the choice of the eigenstates of each doublet. The coefficients a_M^n for the four doublets with the lowest energy are given in Table 9.7. The expectation values $\langle\psi_n|J_z|\psi_n\rangle$ between the eigenstates quoted in Table 9.7 are given by 1.903, -1.903, 5.995, -5.995, 0.586, -0.586, 0.028 and -0.028 for $n = 1, 2, \ldots$ and 8, respectively. Note that all the expectation values differ considerably from the saturation value $\frac{15}{2}$.

Now we evaluate the effective magnetic moments of the lowest energy doublet. Indeed, as one can see from Eq. (9.4.44), the excited doublets are more than 100 K higher in energy so that they do not contribute to the thermodynamic properties at temperatures $T \lesssim 1\,\text{K}$ where the ordered magnetic phase exists.[79] Using the second

Table 9.7. Eigenvectors belonging to the lower eigenvalues given in Eq. (9.4.44).

M	a_M^1	a_M^2	a_M^3	a_M^4	a_M^5	a_M^6	a_M^7	a_M^8
$\frac{15}{2}$	0	0.024	0.828	0	0	0.127	−0.153	0
$\frac{13}{2}$	−0.542	0	0	0.082	0.135	0	0	0.461
$\frac{11}{2}$	0	−0.276	−0.052	0	0	−0.119	−0.412	0
$\frac{9}{2}$	0.003	0	0	0.048	−0.254	0	0	0.059
$\frac{7}{2}$	0	−0.013	−0.509	0	0	−0.071	0.101	0
$\frac{5}{2}$	0.584	0	0	−0.067	−0.096	0	0	−0.347
$\frac{3}{2}$	0	0.537	0.078	0	0	0.182	−0.636	0
$\frac{1}{2}$	−0.005	0	0	−0.182	0.917	0	0	−0.238
$-\frac{1}{2}$	0	−0.005	−0.182	0	0	0.917	−0.238	0
$-\frac{3}{2}$	0.537	0	0	0.078	0.182	0	0	0.636
$-\frac{5}{2}$	0	0.584	−0.067	0	0	−0.096	−0.347	0
$-\frac{7}{2}$	−0.013	0	0	−0.509	−0.071	0	0	0.101
$-\frac{9}{2}$	0	0.003	0.048	0	0	−0.254	0.059	0
$-\frac{11}{2}$	−0.276	0	0	−0.052	−0.119	0	0	−0.412
$-\frac{13}{2}$	0	−0.542	0.082	0	0	0.135	0.461	0
$-\frac{15}{2}$	0.024	0	0	0.828	0.127	0	0	−0.153

and third column of Table 9.7, one finds

$$\langle\psi_1|J_z|\psi_1\rangle = -\langle\psi_2|J_z|\psi_2\rangle = 1.903, \quad \langle\psi_1|J_z|\psi_2\rangle = \langle\psi_2|J_z|\psi_1\rangle = 0 \tag{9.4.46}$$

so that one can write

$$J_z = 3.807\, S_z \Rightarrow \mu_z = g_J \mu_B J_z = 4.568 \mu_B S_z, \tag{9.4.47}$$

where $S_z = \frac{1}{2}\sigma_z$, σ_z being one of the Pauli matrices, and the Landé factor $g_J = \frac{6}{5}$ is obtained using $J = \frac{15}{2}$, $L = 6$, $S = \frac{3}{2}$. The matrix elements of the raising and lowering angular momentum operators in the ground-state doublet are given by

$$\langle\psi_1|J_+|\psi_1\rangle = \langle\psi_2|J_+|\psi_2\rangle = 0, \quad \langle\psi_1|J_+|\psi_2\rangle = 6.442, \quad \langle\psi_2|J_+|\psi_1\rangle = -0.262 \tag{9.4.48}$$

and

$$\langle\psi_1|J_-|\psi_1\rangle = \langle\psi_2|J_-|\psi_2\rangle = 0, \quad \langle\psi_1|J_-|\psi_2\rangle = -0.262, \quad \langle\psi_2|J_-|\psi_1\rangle = 6.442 \tag{9.4.49}$$

leading to

$$J_x = \frac{1}{2}\,(J_+ + J_-) = 6.180\,S_x \Rightarrow \mu_x = g_J\mu_B J_x = 7.416\mu_B S_x \tag{9.4.50}$$

and

$$J_y = \frac{1}{2i}(J_+ - J_-) = 6.703\,S_y \Rightarrow \mu_x = g_J\mu_B J_y = 8.044\mu_B S_y, \tag{9.4.51}$$

where $S_x = \frac{1}{2}\sigma_x$ and $S_y = \frac{1}{2}\sigma_y$, σ_x and σ_y being the remaining two Pauli matrices. The principal information we receive from this calculation is that the presence of the surrounding oxygen ions removes the 16-fold degeneracy of the ground-state multiplet ($J = \frac{15}{2}$) of the "free" Er^{3+} leading to a ground-state doublet ($S = \frac{1}{2}$) with anisotropic Landé factors[86] $g_{xx} = 7.416$, $g_{yy} = 8.044$ and $g_{zz} = 4.568$. As a consequence, the dipolar energy (9.1.11) becomes

$$E^{\alpha}_{\rm dip}(\boldsymbol{G}/2) = -\frac{(g_{\alpha\alpha}\mu_B S)^2}{2} N D^{\alpha\alpha}_V(\boldsymbol{G}/2), \tag{9.4.52}$$

where $\alpha = x, y, z$, $S = \frac{1}{2}$ and $D^{\alpha\alpha}_V(\boldsymbol{G}/2)$ are given in Table 9.2 for $ErBa_2Cu_3O_7$. In particular, taking $a = 3.82\,$Å and measuring the energy in Kelvin degrees one has

$$\begin{aligned} E^{x}_{\rm dip}(\boldsymbol{G}/2)/(k_B N) &= -0.0768\,[a^3 D^{xx}_V(\boldsymbol{G}/2)], \\ E^{y}_{\rm dip}(\boldsymbol{G}/2)/(k_B N) &= -0.0904\,[a^3 D^{yy}_V(\boldsymbol{G}/2)], \\ E^{z}_{\rm dip}(\boldsymbol{G}/2)(k_B N) &= -0.0292[a^3 D^{zz}_V(\boldsymbol{G}/2)]. \end{aligned} \tag{9.4.53}$$

Looking at the values of $a^3 D^{\alpha\alpha}_V(\boldsymbol{G}/2)$ of Table 9.2 we conclude that the CEF due to the surrounding oxygen leads to a ground state corresponding to the configurations $(\frac{1}{2}, 0, \frac{1}{2})$ or $(\frac{1}{2}, 0, 0)$ (very close in energy) with the spins directed along the ferromagnetic b-axis in agreement with the experiment.[79] Note that these configurations become stable only for $g_{yy}/g_{xx} > 1.018$ as one can deduce from Eq. (9.4.53) and Table 9.2. For $g_{yy}/g_{xx} < 1.018$, the ground-state configurations are again those shown in Fig. 9.2. The lowest dipolar energy (9.4.53) becomes $E^{y}_{\rm dip}(\frac{1}{2}, 0, \frac{1}{2})/(k_B N) = -0.442\,$K, of the order of magnitude of the transition temperature $T_N = 0.62\,$K. Moreover, the sublattice magnetization that corresponds to the square root of the intensity of the elastic peak at $(\frac{1}{2}, 0, \frac{1}{2})$ is seen to vanish at the transition following the power law $M_s \sim (T_N - T)^{1/8}$ that corresponds to the critical behaviour of a 2D, $S = \frac{1}{2}$ Ising model. This result is in agreement with the CEF calculation that leads to a ground state with an effective spin $S = \frac{1}{2}$ and uniaxial (Ising) anisotropy. The 2D character is explained by the large ratio $c/a \sim 3$ while the critical exponent of the order parameter $\beta = \frac{1}{8}$ is the exact result for a 2D, $S = \frac{1}{2}$ Ising model with NN exchange interaction.

The tetragonal symmetry ($a = b$) of the deoxygenated non-superconducting compound $ErBa_2Cu_3O_6$ reduces the number of terms of the CEF Hamiltonian (9.4.20). In particular, from Eqs. (9.4.12), (9.4.14), (9.4.17) and (9.4.19) one can see that $A_2^{\pm 2}{=}A_4^{\pm 2}{=}A_6^{\pm 2}{=}A_6^{\pm 6}{=}0$ and the best fit of the remaining non-zero parameters obtained from the INS[80] gives

$$\begin{gathered} B_2^0 = 1.6 \times 10^{-2}, \quad B_4^0 = -1.49 \times 10^{-3}, \quad B_6^0 = 7.39 \times 10^{-6}, \\ B_4^4 = 6.94 \times 10^{-3}, \quad B_6^4 = 2.16 \times 10^{-4}. \end{gathered} \tag{9.4.54}$$

The energy levels of the CEF Hamiltonian become

$$\begin{aligned} E_1 = E_2 &= -41.00\,\text{meV} \Rightarrow E_{1,2}/k_B = 0\,\text{K}, \\ E_3 = E_4 &= -33.21\,\text{meV} \Rightarrow E_{3,4}/k_B = 90\,\text{K}, \\ E_5 = E_6 &= -29.64\,\text{meV} \Rightarrow E_{5,6}/k_B = 132\,\text{K}, \\ E_7 = E_8 &= -29.07\,\text{meV} \Rightarrow E_{7,8}/k_B = 138\,\text{K}, \\ E_9 = E_{10} &= 28.03\,\text{meV} \Rightarrow E_{9,10}/k_B = 801\,\text{K}, \\ E_{11} = E_{12} &= 31.32\,\text{meV} \Rightarrow E_{11,12}/k_B = 839\,\text{K}, \\ E_{13} = E_{14} &= 34.62\,\text{meV} \Rightarrow E_{13,14}/k_B = 878\,\text{K}, \\ E_{15} = E_{16} &= 38.95\,\text{meV} \Rightarrow E_{15,16}/k_B = 928\,\text{K}. \end{aligned} \tag{9.4.55}$$

The two eigenstates belonging to the ground-state doublet are given by

$$|\psi_1\rangle = -0.558|13/2\rangle + 0.589|5/2\rangle + 0.520|-3/2\rangle - 0.266|-11/2\rangle \tag{9.4.56}$$

and

$$|\psi_2\rangle = -0.266|11/2\rangle + 0.520|3/2\rangle + 0.589|-5/2\rangle - 0.558|-13/2\rangle. \tag{9.4.57}$$

From the eigenstates (9.4.56) and (9.4.57), one obtains

$$J_z = 4.198\,S_z \Rightarrow \mu_z = g_J \mu_B J_z = 5.038 \mu_B S_z, \tag{9.4.58}$$

$$J_x = 6.318\,S_x \Rightarrow \mu_x = g_J \mu_B J_x = 7.581 \mu_B S_x \tag{9.4.59}$$

and

$$J_y = 6.318\,S_y \Rightarrow \mu_y = g_J \mu_B J_y = 7.581 \mu_B S_y \tag{9.4.60}$$

so that $g_{zz} = g_{\parallel} = 5.038$, $g_{xx} = g_{yy} = g_{\perp} = 7.162$. The easy-plane character of the anisotropy does not modify the scenario obtained from the dipole–dipole interaction for a free ion. The two ground-state configurations deduced by Table 9.3 correspond to the wavevectors $(0, \frac{1}{2}, \frac{1}{2})$ and $(\frac{1}{2}, 0, \frac{1}{2})$ with the spins directed along the ferromagnetic axis (a for the former, b for the latter ground state). The INS experiment[79] on $ErBa_2Cu_3O_{6+x}$ with $x < 0.3$ rules out the existence of 3D LRO down to $T = 0.06\,\text{K}$. The 2D short range order corresponds to a ridge $\boldsymbol{Q} = (\frac{1}{2}, 0, q)$ with $0 < q < \frac{1}{2}$ with the spins in the ab-plane. The absence of LRO contrasts with the CEF and dipolar energy calculation that lead to a ground-state doublet

that supports the existence of LRO. The specific-heat data[87] confirm the 2D, $S = \frac{1}{2}$ Ising-like behaviour for the (ordered) orthorhombic compound. On the contrary, the data indicate a 2D, planar rotator model behaviour for the (disordered) tetragonal compound.

9.5. Spin Waves in $ErBa_2Cu_3O_7$

To get the spin wave spectrum of $ErBa_2Cu_3O_7$, we make use of the transformation (7.1.2) assuming $\theta = \frac{\pi}{2}$, $\phi = \frac{\pi}{2}$, $\boldsymbol{Q} \equiv \frac{\boldsymbol{G}}{2} = (\frac{1}{2}, 0, \frac{1}{2})$, $g_{xx} = 7.416$, $g_{yy} = 8.044$ and $g_{zz} = 4.568$ corresponding to the ground-state configuration of $ErBa_2Cu_3O_7$. In this way, the transformation (7.1.2) reduces to

$$S_i^x = -S_i^\eta \cos\frac{\boldsymbol{G}\cdot\boldsymbol{r}_i}{2}, \quad S_i^y = S_i^\zeta \cos\frac{\boldsymbol{G}\cdot\boldsymbol{r}_i}{2}, \quad S_i^z = -S_i^\xi. \tag{9.5.1}$$

Then the spin-boson transformation

$$\begin{aligned} S_i^\xi &= \frac{\sqrt{2S}}{2}(a_i + a_i^+), \\ S_i^\eta &= \frac{\sqrt{2S}}{2i}(a_i - a_i^+), \\ S_i^\zeta &= S - a_i^+ a_i \end{aligned} \tag{9.5.2}$$

can be used to write the harmonic Hamiltonian

$$\begin{aligned} \mathcal{H}_2^{\rm dip} = & E_{\rm dip}^y\left(\frac{\boldsymbol{G}}{2}\right) + \sum_{\boldsymbol{q}} A_{\boldsymbol{q}}^{\rm dip}\, a_{\boldsymbol{q}}^+ a_{\boldsymbol{q}} + \frac{1}{2}\sum_{\boldsymbol{q}} B_{\boldsymbol{q}}^{\rm dip}\,(a_{\boldsymbol{q}} a_{-\boldsymbol{q}} + a_{\boldsymbol{q}}^+ a_{-\boldsymbol{q}}^+) \\ & + \frac{1}{2}\sum_{\boldsymbol{q}} iC_{\boldsymbol{q}}^{\rm dip}\left(a_{\boldsymbol{q}} a_{-\boldsymbol{q}-\frac{\boldsymbol{G}}{2}} - a_{\boldsymbol{q}}^+ a_{-\boldsymbol{q}-\frac{\boldsymbol{G}}{2}}^+\right) + \frac{1}{2}\sum_{\boldsymbol{q}} iD_{\boldsymbol{q}}^{\rm dip}\left(a_{\boldsymbol{q}}^+ a_{\boldsymbol{q}+\frac{\boldsymbol{G}}{2}} - a_{\boldsymbol{q}+\frac{\boldsymbol{G}}{2}}^+ a_{\boldsymbol{q}}\right), \end{aligned} \tag{9.5.3}$$

where

$$E_{\rm dip}^y\left(\frac{\boldsymbol{G}}{2}\right) = -\frac{1}{2}(g_{yy}\mu_B S)^2 N D^{yy}\left(\frac{\boldsymbol{G}}{2}\right), \tag{9.5.4}$$

$$A_{\boldsymbol{q}}^{\rm dip} = \frac{1}{2}\mu_B^2 S\left[2g_{yy}^2 D^{yy}\left(\frac{\boldsymbol{G}}{2}\right) - g_{xx}^2 D^{xx}\left(\frac{\boldsymbol{G}}{2}+\boldsymbol{q}\right) - g_{zz}^2 D^{zz}(\boldsymbol{q})\right], \tag{9.5.5}$$

$$B_{\boldsymbol{q}}^{\rm dip} = \frac{1}{2}\mu_B^2 S\left[g_{xx}^2 D^{xx}\left(\frac{\boldsymbol{G}}{2}+\boldsymbol{q}\right) - g_{zz}^2 D^{zz}(\boldsymbol{q})\right], \tag{9.5.6}$$

$$C_{\boldsymbol{q}}^{\rm dip} = \frac{1}{2}\mu_B^2 S g_{xx} g_{zz}\left[D^{xz}(\boldsymbol{q}) + D^{xz}\left(\boldsymbol{q}+\frac{\boldsymbol{G}}{2}\right)\right] \tag{9.5.7}$$

and

$$D_{\boldsymbol{q}}^{\rm dip} = \frac{1}{2}\mu_B^2 S g_{xx} g_{zz}\left[D^{xz}\left(\boldsymbol{q}+\frac{\boldsymbol{G}}{2}\right) - D^{xz}(\boldsymbol{q})\right]. \tag{9.5.8}$$

To obtain Eq. (9.5.3), we have made use of the properties $C_{\boldsymbol{q}+\frac{\boldsymbol{G}}{2}}^{\rm dip} = C_{\boldsymbol{q}}^{\rm dip}$ and $D_{\boldsymbol{q}+\frac{\boldsymbol{G}}{2}}^{\rm dip} = -D_{\boldsymbol{q}}^{\rm dip}$ coming from Eqs. (9.5.7) and (9.5.8) and of the fact that $\boldsymbol{G}$ is

a reciprocal lattice vector. The Hamiltonian (9.5.3) can be diagonalised using the same procedure of Section 7.9. The transformation

$$\alpha_{\boldsymbol{k}}^{(i)} = u_{\boldsymbol{k}}^{(i)} a_{\boldsymbol{k}} - l_{\boldsymbol{k}}^{(i)} a_{-\boldsymbol{k}}^{+} + v_{\boldsymbol{k}}^{(i)} a_{\boldsymbol{k}+\frac{\boldsymbol{G}}{2}} - m_{\boldsymbol{k}}^{(i)} a_{-\boldsymbol{k}-\frac{\boldsymbol{G}}{2}}^{+} \tag{9.5.9}$$

with

$$|u_{\boldsymbol{k}}^{(i)}|^2 - |l_{\boldsymbol{k}}^{(i)}|^2 + |v_{\boldsymbol{k}}^{(i)}|^2 - |m_{\boldsymbol{k}}^{(i)}|^2 = 1 \tag{9.5.10}$$

and

$$u_{-\boldsymbol{k}}^{(i)} = u_{\boldsymbol{k}}^{(i)*}, \quad l_{-\boldsymbol{k}}^{(i)} = l_{\boldsymbol{k}}^{(i)*}, \quad v_{-\boldsymbol{k}} = v_{\boldsymbol{k}}^{(i)*}, \quad m_{-\boldsymbol{k}}^{(i)} = m_{\boldsymbol{k}}^{(i)*} \tag{9.5.11}$$

brings the Hamiltonian (9.5.3) into the form

$$\mathcal{H}_2 = E_0' + \sum_i \sum_{\boldsymbol{k}} \hbar\omega_{\boldsymbol{k}}^{(i)*} \alpha_{\boldsymbol{k}}^{(i)+} \alpha_{\boldsymbol{k}}^{(i)} \tag{9.5.12}$$

where the frequencies $\omega_{\boldsymbol{k}}^{(i)}$ are the solutions of the determinant equation

$$\det \begin{pmatrix} A_{\boldsymbol{k}} - \hbar\omega_{\boldsymbol{k}}^{(i)} & B_{\boldsymbol{k}} & -iD_{\boldsymbol{k}} & iC_{\boldsymbol{k}} \\ B_{\boldsymbol{k}} & A_{\boldsymbol{k}} + \hbar\omega_{\boldsymbol{k}}^{(i)} & -iC_{\boldsymbol{k}} & iD_{\boldsymbol{k}} \\ iD_{\boldsymbol{k}} & iC_{\boldsymbol{k}} & A_{\boldsymbol{k}+\frac{\boldsymbol{G}}{2}} - \hbar\omega_{\boldsymbol{k}}^{(i)} & B_{\boldsymbol{k}+\frac{\boldsymbol{G}}{2}} \\ -iC_{\boldsymbol{k}} & -iD_{\boldsymbol{k}} & B_{\boldsymbol{k}+\frac{\boldsymbol{G}}{2}} & A_{\boldsymbol{k}+\frac{\boldsymbol{G}}{2}} + \hbar\omega_{\boldsymbol{k}}^{(i)} \end{pmatrix} = 0. \tag{9.5.13}$$

In Eq. (9.5.13) we have dropped the superscript "dip" occurring in Eq. (9.5.3). The determinant equation (9.5.13) leads to a biquadratic equation in the variable $\hbar\omega_{\boldsymbol{k}}^{(i)}$ whose positive (physical) solutions are[86]

$$\begin{aligned} \hbar\omega_{\boldsymbol{k}}^{(1,2)} = \Bigg\{ & \frac{1}{2}(A_{\boldsymbol{k}}^2 - B_{\boldsymbol{k}}^2 + A_{\boldsymbol{k}+\frac{\boldsymbol{G}}{2}}^2 - B_{\boldsymbol{k}+\frac{\boldsymbol{G}}{2}}^2) - C_{\boldsymbol{k}}^2 + D_{\boldsymbol{k}}^2 \\ & \pm \Bigg[\frac{1}{4}(A_{\boldsymbol{k}}^2 - B_{\boldsymbol{k}}^2 - A_{\boldsymbol{k}+\frac{\boldsymbol{G}}{2}}^2 + B_{\boldsymbol{k}+\frac{\boldsymbol{G}}{2}}^2)^2 - C_{\boldsymbol{k}}^2 \left((A_{\boldsymbol{k}} - A_{\boldsymbol{k}+\frac{\boldsymbol{G}}{2}})^2 \right. \\ & \left. - (B_{\boldsymbol{k}} - B_{\boldsymbol{k}+\frac{\boldsymbol{G}}{2}})^2 \right) + D_{\boldsymbol{k}}^2 \left((A_{\boldsymbol{k}} - A_{\boldsymbol{k}+\frac{\boldsymbol{G}}{2}})^2 - (B_{\boldsymbol{k}} - B_{\boldsymbol{k}+\frac{\boldsymbol{G}}{2}})^2 \right) \\ & + 4C_{\boldsymbol{k}} D_{\boldsymbol{k}} \left(A_{\boldsymbol{k}} B_{\boldsymbol{k}+\frac{\boldsymbol{G}}{2}} - A_{\boldsymbol{k}+\frac{\boldsymbol{G}}{2}} B_{\boldsymbol{k}} \right) \Bigg]^{\frac{1}{2}} \Bigg\}^{\frac{1}{2}}. \end{aligned} \tag{9.5.14}$$

A considerable simplification of Eq. (9.5.14) is obtained by taking $C_{\boldsymbol{k}} = D_{\boldsymbol{k}} = 0$. This assumption is rigorously true for wavevectors $\boldsymbol{k}$ parallel to the high symmetry directions where $D^{xz}(\boldsymbol{k}) = 0$ (see Eqs. (9.5.7) and (9.5.8)). For $\boldsymbol{k} = (\frac{2\pi}{a}h, \frac{2\pi}{b}h, 1.3\frac{2\pi}{c}) \equiv (h, h, 1.3)$ (r.l.u), the scattering vectors used in the INS experiment[68], $D^{xz}(\boldsymbol{k})$ is not zero but its value is so small that the difference between

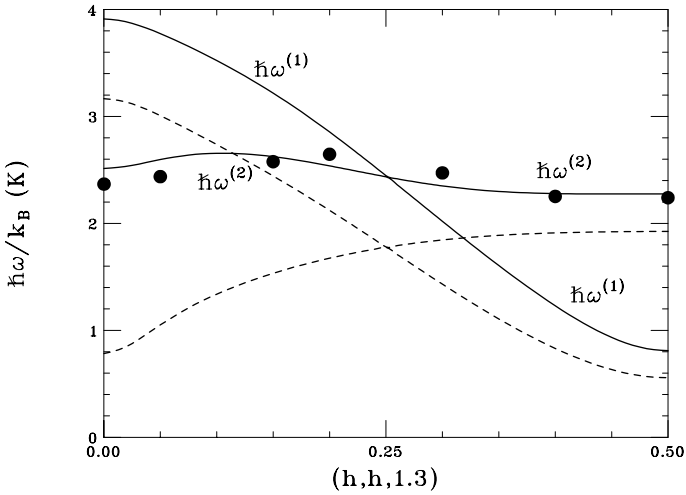

Fig. 9.4. Spin wave spectra $\hbar\omega^{(1)}/k_B$ (Eq. 9.5.15) and $\hbar\omega^{(2)}/k_B$ (Eq. 9.5.16) along $\boldsymbol{k} = (h, h, 1.3)$ (r.l.u.) for $ErBa_2Cu_3O_7$. The dashed curves are obtained for a pure dipolar model with $g_{xx} = 7.416$, $g_{yy} = 8.044$ and $g_{zz} = 4.568$. The continuous curves are obtained for a model with dipolar and exchange interaction ($J_{\rm NN} = 0.0054$ K, $J'_{\rm NN} = 0.05 J_{\rm NN}$ and $J_{\rm NNN} = 0.45 J_{\rm NN}$). The full circles are the experimental data obtained from the INS[88] on $ErBa_2Cu_3O_7$.

the spin wave frequencies with and without $C_{\boldsymbol{k}}$ and $D_{\boldsymbol{k}}$ cannot be appreciated in Fig. 9.4 where the dash curves show the magnon spectra given by

$$\hbar\omega^{(1)}_{\boldsymbol{k}} = \sqrt{A^2_{\boldsymbol{k}} - B^2_{\boldsymbol{k}}} \tag{9.5.15}$$

and

$$\hbar\omega^{(2)}_{\boldsymbol{k}} = \sqrt{A^2_{\boldsymbol{k}+\frac{\boldsymbol{G}}{2}} - B^2_{\boldsymbol{k}+\frac{\boldsymbol{G}}{2}}} \tag{9.5.16}$$

obtained from Eq. (9.5.14) putting $C_{\boldsymbol{k}} = D_{\boldsymbol{k}} = 0$.

As one can see, the experimental data (full circles) are not recovered. We try to recover the experimental data by introducing a weak exchange interaction between the Er^{3+} ions represented by the Hamiltonian

$$\begin{aligned}\mathcal{H}^{\rm ex} = &\sum_{i,\boldsymbol{\delta}_{\rm NN}} \sum_{\alpha} g^2_{\alpha\alpha} J_{\rm NN} S^{\alpha}_i S^{\alpha}_{i+\boldsymbol{\delta}_{\rm NN}} + \sum_{i,\boldsymbol{\delta}'_{\rm NN}} \sum_{\alpha} g^2_{\alpha\alpha} J'_{\rm NN} S^{\alpha}_i S^{\alpha}_{i+\boldsymbol{\delta}'_{\rm NN}} \\ &+ \sum_{i,\boldsymbol{\delta}_{\rm NNN}} \sum_{\alpha} g^2_{\alpha\alpha} J_{\rm NNN} S^{\alpha}_i S^{\alpha}_{i+\boldsymbol{\delta}_{\rm NNN}},\end{aligned} \tag{9.5.17}$$

where $J_{\rm NN}$ is the in-plane NN interaction with $\boldsymbol{\delta}_{\rm NN} = (\pm a, 0, 0)$ and $(0, \pm b, 0)$, $J'_{\rm NN}$ is the out-of-plane NN interaction with $\boldsymbol{\delta}'_{\rm NN} = (0, 0, \pm c)$ and $J_{\rm NNN}$ is the in-plane NNN interaction with $\boldsymbol{\delta}_{\rm NNN} = (\pm a, \pm b, 0)$. At variance with the isotropic Heisenberg Hamiltonian, the factors $g_{\alpha\alpha}$ with $\alpha = x, y, z$ occur in Eq. (9.5.17) in agreement with the CEF calculation of the previous section. Using the spin-boson

transformation (9.5.2), from Eq. (9.5.17) one obtains the harmonic Hamiltonian

$$\mathcal{H}^{\rm ex} = NS^2 g_{yy}^2 J\left(\frac{\boldsymbol{G}}{2}\right) + \sum_{\boldsymbol{q}} A_{\boldsymbol{q}}^{\rm ex}\ a_{\boldsymbol{q}}^{+} a_{\boldsymbol{q}} + \frac{1}{2}\sum_{\boldsymbol{q}} B_{\boldsymbol{q}}^{\rm ex}(a_{\boldsymbol{q}} a_{-\boldsymbol{q}} + a_{\boldsymbol{q}}^{+} a_{-\boldsymbol{q}}^{+}) \tag{9.5.18}$$

where

$$A_{\boldsymbol{q}}^{\rm ex} = S\left[g_{xx}^2 J\left(\boldsymbol{q}+\frac{\boldsymbol{G}}{2}\right) + g_{zz}^2 J(\boldsymbol{q}) - 2g_{yy}^2 J\left(\frac{\boldsymbol{G}}{2}\right)\right], \tag{9.5.19}$$

$$B_{\boldsymbol{q}}^{\rm ex} = S\left[g_{zz}^2 J(\boldsymbol{q}) - g_{xx}^2 J\left(\boldsymbol{q}+\frac{\boldsymbol{G}}{2}\right)\right] \tag{9.5.20}$$

with

$$J(\boldsymbol{q}) = 2J_{\rm NN}(\cos aq_x + \cos bq_y) + 2J'_{\rm NN}\cos cq_z + 4J_{\rm NNN}\cos aq_x \cos bq_y. \tag{9.5.21}$$

Note that from the lattice parameters of $ErBa_2Cu_3O_7$ ($c \sim 3a$ and $b \sim a$) one expects that $J_{\rm NN} > J_{\rm NNN} > J'_{\rm NN}$. The only effect of a weak antiferromagnetic coupling $J'_{\rm NN} > 0$ is to stabilize the antiferromagnetic ordering along the c-axis while the introduction of a NNN in-plane antiferromagnetic interaction $J_{\rm NNN} > 0$ favours a columnar order, competing with the NN in-plane antiferromagnetic interaction $J_{\rm NN} > 0$ that supports a Néel order. The ground-state configuration of $ErBa_2Cu_3O_7$, corresponding to $\boldsymbol{G} = (\frac{1}{2}, 0, \frac{1}{2})$, imposes an upper limit to $J_{\rm NN}$ that can be obtained comparing the ground-state energy of the configuration really observed with the Néel configuration supported by the dominant antiferromagnetic exchange interaction. Indeed, imposing that $E_{\rm dip}^{y}(\frac{1}{2}, 0, \frac{1}{2}) + NS^2 g_{yy}^2 J(\frac{1}{2}, 0, \frac{1}{2}) < E_{\rm dip}^{z}(\frac{1}{2}, \frac{1}{2}, \frac{1}{2}) + NS^2 g_{zz}^2 J(\frac{1}{2}, \frac{1}{2}, \frac{1}{2})$ and using $g_{yy} = 8.044$, $g_{zz} = 4.568$, one obtains

$$J_{\rm NN} < 0.0176 + 1.050\, J'_{\rm NN} + 4.101\, J_{\rm NNN}\ \ ({\rm K}). \tag{9.5.22}$$

The spin wave spectra including the exchange interaction are still given by Eqs. (9.5.15) and Eq. (9.5.14) with $A_{\boldsymbol{k}} = A_{\boldsymbol{k}}^{\rm dip} + A_{\boldsymbol{k}}^{\rm ex}$ and $B_{\boldsymbol{k}} = B_{\boldsymbol{k}}^{\rm dip} + B_{\boldsymbol{k}}^{\rm ex}$. The continuous curves of Fig. 9.4 show the spin wave spectra for $J_{\rm NN} = 0.0054$ K, $J' = 0.05\, J_{\rm NN}$ and $J_{\rm NNN} = 0.45 J_{\rm NN}$. The agreement of $\hbar\omega_{\boldsymbol{k}}^{(2)}$ with the experimental data is excellent. The choice of the exchange parameters is not unique: indeed, for $0.0045 \lesssim J_{\rm NN} \lesssim 0.0063\,{\rm K}$, the agreement with the experimental data remains good provided that the value of $J_{\rm NNN}$ is correspondingly changed.[86] The main discrepancy between the theory and the experiment pointed out in Fig. 9.4 is that the experimental data[88] fall on a unique branch. In order to understand why the INS cross-section leads to such a result, it becomes important to evaluate explicitly the neutron scattering cross-section for the model taken to fit experimental data. Using the spin wave spectra (9.5.15) and (9.5.16), the INS cross-section may be obtained

in the same manner as in Section 7.10. One has

$$\left(\frac{d^2\sigma}{d\Omega\ dE'}\right)_{\text{inel}} = r_0^2\frac{k'}{k}\left[\frac{1}{2}F(\boldsymbol{K})\right]^2 e^{-2W(\boldsymbol{K})}\frac{SN}{2\hbar}\left\{I^{xx}(\boldsymbol{K})\left[(1+n^{(2)})\delta(\omega-\omega_{\boldsymbol{K}}^{(2)})\right.\right.$$
$$\left.\left.+\,n^{(2)}\delta(\omega+\omega_{\boldsymbol{K}}^{(2)})\right]+I^{zz}(\boldsymbol{K})\left[(1+n^{(1)})\delta(\omega-\omega_{\boldsymbol{K}}^{(1)})+n_1\delta(\omega+\omega_{\boldsymbol{K}}^{(1)})\right]\right\}, \tag{9.5.23}$$

where

$$I^{xx}(\boldsymbol{K}) = g_{xx}^2\left(1-\frac{K_x^2}{K^2}\right)\left[\frac{A_{\boldsymbol{K}+\frac{\boldsymbol{G}}{2}}-|B_{\boldsymbol{K}+\frac{\boldsymbol{G}}{2}}|}{A_{\boldsymbol{K}+\frac{\boldsymbol{G}}{2}}+|B_{\boldsymbol{K}+\frac{\boldsymbol{G}}{2}}|}\right]^{\frac{1}{2}}, \tag{9.5.24}$$

$$I^{zz}(\boldsymbol{K}) = g_{zz}^2\left(1-\frac{K_z^2}{K^2}\right)\left[\frac{A_{\boldsymbol{K}}+|B_{\boldsymbol{K}}|}{A_{\boldsymbol{K}}-|B_{\boldsymbol{K}}|}\right]^{\frac{1}{2}} \tag{9.5.25}$$

and

$$n^{(i)} = \frac{1}{e^{\beta\hbar\omega_{\boldsymbol{K}}^{(i)}}-1}. \tag{9.5.26}$$

In Table 9.8, we give the peak intensities $I^{zz}(\boldsymbol{K})$ and $I^{xx}(\boldsymbol{K})$ along with the related frequencies $\omega_{\boldsymbol{K}}^{(1)}$ and $\omega_{\boldsymbol{K}}^{(2)}$ for $g_{xx}=7.416, g_{zz}=4.568, b/a=1.016, c/a=3.052$ and scattering vectors $\boldsymbol{K}=(h,h,1.3)$. As one can see, the peak intensity $I^{xx}(\boldsymbol{K})$ corresponding to the branch $\omega_{\boldsymbol{K}}^{(2)}$ is greater than $I^{zz}(\boldsymbol{K})$ corresponding to the branch $\omega_{\boldsymbol{K}}^{(1)}$ for any $\boldsymbol{K}$ except near the zone boundary. This is due to the geometric factor $(1-K_x^2/K^2)$ that is greater than $(1-K_z^2/K^2)$ for any h except $h\gtrsim 0.4$. Indeed, by using the parameters chosen in Table 9.8, one has

$$\frac{1-\frac{K_x^2}{K^2}}{1-\frac{K_z^2}{K^2}} = \frac{0.969h^2+0.181}{1.969h^2} \tag{9.5.27}$$

that goes to ∞ for $h\to 0$. In any case, this leads to a different weight of the two peaks in the neutron scattering cross-section even though it does not explain the

Table 9.8. Peak intensity $I^{xx}(\boldsymbol{K})$ and $I^{zz}(\boldsymbol{K})$ and related spin wave energies $\hbar\omega_{\boldsymbol{K}}^{(1)}$ frequencies and $\hbar\omega_{\boldsymbol{K}}^{(2)}$ for selected values of the scattering vector $\boldsymbol{K}=(h,h,1.3)$ (r.l.u.).

h	$I^{zz}(\boldsymbol{K})$	$\hbar\omega_{\boldsymbol{K}}^{(1)}/k_B$ (K)	$I^{xx}(\boldsymbol{K})$	$\hbar\omega_{\boldsymbol{K}}^{(2)}/k_B$ (K)
0	0	3.911	48.518	2.513
0.05	0.563	3.773	46.626	2.599
0.1	2.093	3.522	44.790	2.656
0.15	4.328	3.218	43.979	2.624
0.2	6.704	2.854	43.578	2.538
0.25	8.618	2.446	42.998	2.436
0.3	11.076	2.020	40.638	2.350
0.35	14.983	1.606	38.326	2.299
0.4	20.825	1.229	37.047	2.279
0.45	29.064	0.934	35.438	2.275
0.5	35.358	0.811	33.995	2.276

presence of a single peak in the experiment for $h \gtrsim 0.3$. It should be noted, however, that in any experiment a limited energy resolution prevents the occurrence of δ-functions in the cross-section. In particular, in the neutron scattering cross-section of $ErBa_2Cu_3O_7$ the full width at half maximum (FWHM) of the data points[88] is $\frac{\hbar\Delta\omega}{k_B} \simeq 1.2$ K. Then a rough simulation of the neutron scattering peak profile at low temperature may be obtained from Eq. (9.5.23), neglecting all terms containing Bose factors and replacing the δ-functions by Gaussians like

$$G^{(i)}(\boldsymbol{K},\omega) = \frac{1}{\sigma\sqrt{2\pi}} \exp^{-\frac{(\omega-\omega_{\boldsymbol{K}}^{(i)})^2}{2\sigma^2}}, \tag{9.5.28}$$

where $i = 1, 2$ and $\sigma = \frac{\hbar\Delta\omega}{2k_B\sqrt{\ln 4}} \simeq 0.51$ K according to the energy resolution of the experiment.[88] In Fig. 9.5, the dashed curves are the Gaussians $G^{(1)}$ and $G^{(2)}$ centred at the frequencies $\omega_{\boldsymbol{K}}^{(1)}$ and $\omega_{\boldsymbol{K}}^{(2)}$ multiplied by $I^{zz}(\boldsymbol{K})$ and $I^{xx}(\boldsymbol{K})$, respectively. The continuous curves are the sums of the two Gaussians. As one can see, the existence of a single peak for $h \lesssim 0.3$ is due to the ratio $I^{zz}/I^{xx} \ll 1$, so that the sums of the two Gaussians do not differ substantially from the Gaussian centred at $\omega_{\boldsymbol{K}}^{(2)}$. On the contrary, the existence of a single, even though asymmetric, peak for $h \gtrsim 0.3$ is due to the limited energy resolution comparable with the energy shift of the two spin wave branches.

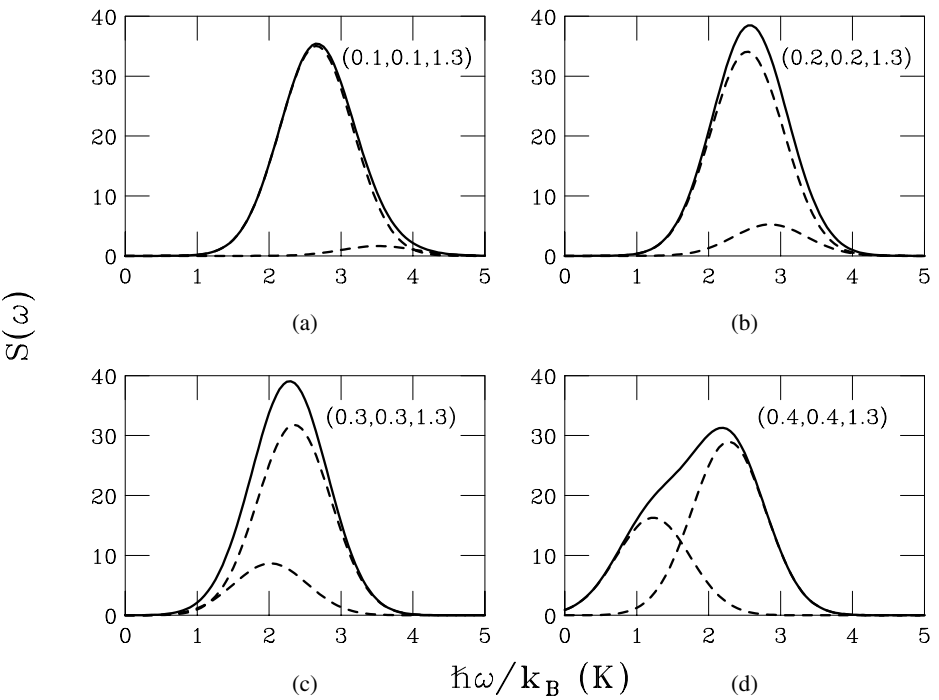

Fig. 9.5. Peak profiles (continuous curve) of the neutron scattering cross-section simulated by the sum of two Gaussians (dashed curves) with FWHM = 1.2 K centred at $\omega_{\boldsymbol{K}}^{(1)}$ and $\omega_{\boldsymbol{K}}^{(2)}$ for selected values of the scattering vector $\boldsymbol{K} = (h, h, 1.3)$: (a) $h = 0.1$; (b) $h = 0.2$; (c) $h = 0.3$; (d) $h = 0.4$.

To summarize, in this section we have tried to indicate what kind of problems must deal with a theoretical physicist when must explain the experimental data of a physical system. Taking $ErBa_2Cu_3O_7$ as an example, we have shown that the dipolar interactions are responsible of the antiferromagnetic configuration of the ground state. The crystalline electric field is essential to obtain at the correct spin orientation. The weak exchange interaction is crucial to recover the spin wave spectrum obtained from the INS cross-section. Finally, the limited energy resolution of the experiment is an important ingredient to describe the INS cross-section profile.